

JGR Space Physics

RESEARCH ARTICLE

10.1029/2022JA030260

Key Points:

- We use 10 years of data from the Time History of Events and Macroscale Interactions during Substorms—Acceleration, Reconnection, Turbulence, and Electrodynamics of the Moon's Interaction with the Sun mission to constrain the lunar plasma environment within the terrestrial magnetotail
- We identify three predominant distributions of the magnetotail plasma, corresponding to the magnetosheath, lobes, and plasma sheet
- For these conditions, we calculate statistical properties of the local magnetic field, plasma bulk velocity, number density, and temperature

Supporting Information:

Supporting Information may be found in the online version of this article.

Correspondence to:

L. Liuzzo,
liuzzo@berkeley.edu

Citation:

Liuzzo, L., Poppe, A. R., & Halekas, J. S. (2022). A statistical study of the Moon's magnetotail plasma environment. *Journal of Geophysical Research: Space Physics*, 127, e2022JA030260. <https://doi.org/10.1029/2022JA030260>

Received 4 JAN 2022
Accepted 19 MAR 2022

A Statistical Study of the Moon's Magnetotail Plasma Environment

Lucas Liuzzo¹ , Andrew R. Poppe¹ , and Jasper S. Halekas² 

¹Space Sciences Laboratory, University of California, Berkeley, Berkeley, CA, USA, ²Department of Physics and Astronomy, University of Iowa, Iowa City, IA, USA

Abstract This study investigates the lunar plasma environment when embedded within Earth's magnetotail. We use data from 10 years of tail crossings by the Acceleration, Reconnection, Turbulence, and Electrodynamics of the Moon's Interaction with the Sun (ARTEMIS) spacecraft in orbit around the Moon. We separate the plasma environments by magnetosheath-like, magnetotail lobe-like, and plasma sheet-like conditions. Our findings highlight that the lobe-like plasma is associated with low densities and a strong magnetic field, while the plasma sheet is characterized by higher densities and a weaker magnetic field. These regions are flanked by the fast, predominantly tailward flows of the terrestrial magnetosheath. During a single lunar crossing, however, the magnetotail displays a wide range of variability, with transient features—including reconnection events—intermixed between periods of lobe-like or sheet-like conditions. We compare and contrast the Moon's local magnetotail plasma to the environments near various outer-planet moons. In doing so, we find that properties of the ambient lunar plasma are, at times, unique to the terrestrial magnetotail, while at others, may resemble those near the Jovian, Saturnian, and Neptunian moons. These findings highlight the complementary role of the ARTEMIS mission in providing a deeper understanding of the plasma interactions of the outer-planet moons.

1. Introduction

During its 29-day orbit, the Moon is exposed to a wide range of plasma environments. While located outside of Earth's magnetosphere, the high density, super-Alfvénic flows of the solar wind continually bombard the Moon. The resulting interaction has been well-studied: an extended wake forms downstream of the Moon (e.g., Michel, 1968; Ness, 1965), characterized by a drop in the solar wind number density and associated with an enhanced magnetic field (Bosqued et al., 1996; Halekas et al., 2015; Holmström et al., 2012; Ness, 1972; Zhang et al., 2014). When located within Earth's magnetosphere, however, the lunar plasma environment is vastly different; after transiting through the shocked magnetosheath plasma, the magnetotail can be characterized by nominally lobe-like and sheet-like plasma (Hardy et al., 1976; Sibeck & Murphy, 2021). Previous studies have applied data from multiple spacecraft missions to study the properties of these plasma populations using a handful of tail crossings. Behannon (1970) used data from the Explorer 33 and Explorer 35 missions to characterize the magnetic field within the tail plasma sheet and found that it is associated with a broad region of reduced magnetic field magnitude that is (on average) oriented northward out to a distance of $70R_E$ (radius of Earth $R_E = 6,378$ km) downstream of the planet. Further studies by, for example, Slavin et al. (1985) and Vasko et al. (2015) have investigated the structure of the tail plasma out to even greater distances of up to $130R_E$, using data from the International Sun-Earth Explorer-3 (ISEE-3) and Geotail missions, respectively. Additional studies of the magnetotail lobes have shown that the plasma typically flows downtail (Hardy et al., 1976) along well-ordered magnetotail lobe field lines mainly oriented sunward/anti-sunward (Meng & Anderson, 1974; Yamamoto et al., 1994); additional components to the magnetotail field are strongly correlated with the direction of the interplanetary magnetic field (e.g., Cowley, 1981a, 1981b; Hardy et al., 1979; Sibeck et al., 1985).

Using these missions to obtain the long-term properties of the lunar magnetotail plasma environment during tail crossings is challenging: the data are restricted by the orbital properties of the spacecraft (e.g., ISEE-3 and Geotail were at times located more than $200R_E$ from Earth) or limited to the brief observational windows when the Moon was located within the magnetotail during the mission's lifetime (e.g., only a few hundred hours of data were collected within the lobes by the instruments placed on the lunar surface during the Apollo missions; see, e.g., Hardy et al. [1976]). Therefore, although the Moon spends approximately a quarter of each lunation

within the terrestrial magnetotail, the statistical properties of the magnetotail plasma along the lunar orbit are only weakly constrained.

Unlike these missions which spent brief periods of time near the Moon's position, the Acceleration, Reconnection, Turbulence, and Electrodynamics of the Moon's Interaction with the Sun (ARTEMIS) mission was placed into lunar orbit (Angelopoulos, 2011). Originally part of the Time History of Events and Macroscale Interactions during Substorms (THEMIS) mission, the two ARTEMIS probes (P1 and P2) have spent more than 10 years exposed to the lunar plasma environment since their orbital insertion in 2011. The goal of this study is therefore to understand the long-term average properties of the Moon's plasma environment while transiting the terrestrial magnetotail using the vast data set obtained during the entire (to date) ARTEMIS mission while the probes were located within Earth's geomagnetic tail. In Section 2, we present data obtained by the probes during a typical tail crossing in order to identify characteristic signatures of the magnetotail plasma. We then present data from 126 tail crossings during the past 10 years of the mission in Section 3, where we investigate properties of the magnetic field, bulk velocity, and density of the local magnetotail plasma, and perform a statistical analysis of the environment to which the Moon is exposed during these crossings. Finally, Section 4 concludes our study and places the lunar plasma environment within the terrestrial magnetotail into a broader context by comparing and contrasting it with the plasma environments near various outer-planet moons.

2. Case Study of a Magnetotail Crossing

The ARTEMIS probes orbit the Moon along elliptical trajectories with periods of approximately 24–26 hr (Angelopoulos, 2011). Each probe has a perilune that varies in altitude from approximately 10 km to 1,000 km, with an apolune on the order of 19,000 km. For this study, we present data from the Flux Gate Magnetometer (FGM; Auster et al., 2008), the Electric Field Instrument (EFI; Bonnell et al., 2008), and the Electrostatic Analyzer (ESA; McFadden, Carlson, Larson, Ludlam, et al. [2008]) collected by the identically instrumented probes.

Before using the ten-year-long ARTEMIS data set to study the properties of the lunar magnetotail environment, we first highlight the key aspects of the various plasma environments to which the Moon is exposed during a typical crossing of the terrestrial magnetotail. For approximately one quarter of each lunation, the Moon (and the two ARTEMIS probes) travels through the Earth's magnetotail at approximately $60R_E$ downstream of the planet. Figure 1 displays ARTEMIS P1 observations from midnight on 24 October 2012 to midnight on 03 November 2012, during such a passage. The magnetosphere during this period was relatively calm, with estimated Planetary K and A indices between $0 \leq K_p \leq 4$ and $2 \leq A_p \leq 17$. Shown from top to bottom in Figure 1 are measurements of the magnetic field \mathbf{B} , the ion and electron differential energy fluxes, the plasma number density n calculated using the reduced electron density product from the ESA, the ion bulk velocity \mathbf{V} , the ion and electron temperatures, the plasma beta, and the Alfvénic Mach number M_A as observed by ARTEMIS. Here, the Alfvénic Mach number is the ratio between the magnitudes of the bulk plasma flow velocity and the Alfvén velocity (given by $V_A = B/\sqrt{nm\mu_0}$ with mass m), while the plasma beta is given by $\beta = 2\mu_0 n k_B T / |\mathbf{B}|^2$. Note that for this study, we assume that all ions detected within the magnetotail are protons with mass $m = 1$ amu. For times where the ESA detects only background ion counts, the total plasma beta displayed in Figure 1 is assumed to equal the electron plasma beta. The solid black line over-plotted onto the electron spectra denotes the spacecraft potential; fluxes below this line are dominated by spacecraft photoelectrons and are thus not geophysical (see McFadden, Carlson, Larson, Bonnell, et al., 2008).

In Figure 1 and for the remainder of the study, components of vector quantities are given in the Geocentric Solar Ecliptic (GSE) coordinate system. In this system, the unit vector $+\hat{\mathbf{z}}$ is parallel with the (upward) normal to Earth's ecliptic plane, $+\hat{\mathbf{x}}$ points Sunward, and $+\hat{\mathbf{y}}$ completes the right-handed set. Note that to ensure accurate calculations of the plasma moments, times when the ARTEMIS ion ESA detected only background counts have been removed from Figure 1, which we define as an integrated ion energy flux below $1.5 \cdot 10^5 \text{ eV cm}^{-2} \text{ s}^{-1} \text{ sr}^{-1}$ (corresponding to a number density on the order of $n \approx 0.01 \text{ cm}^{-3}$). In addition, we have removed measurements obtained when the P1 probe was located within the Moon's shadow from the data set, which affects the accuracy of the magnetic field vector and the particle moments (see Georgescu et al., 2011), as well as measurements within $0.5R_M$ of the Moon's surface ($R_M = 1,737 \text{ km}$) in order to exclude any lunar perturbations on the local plasma environment (e.g., Halekas et al., 2013; Poppe et al., 2012).

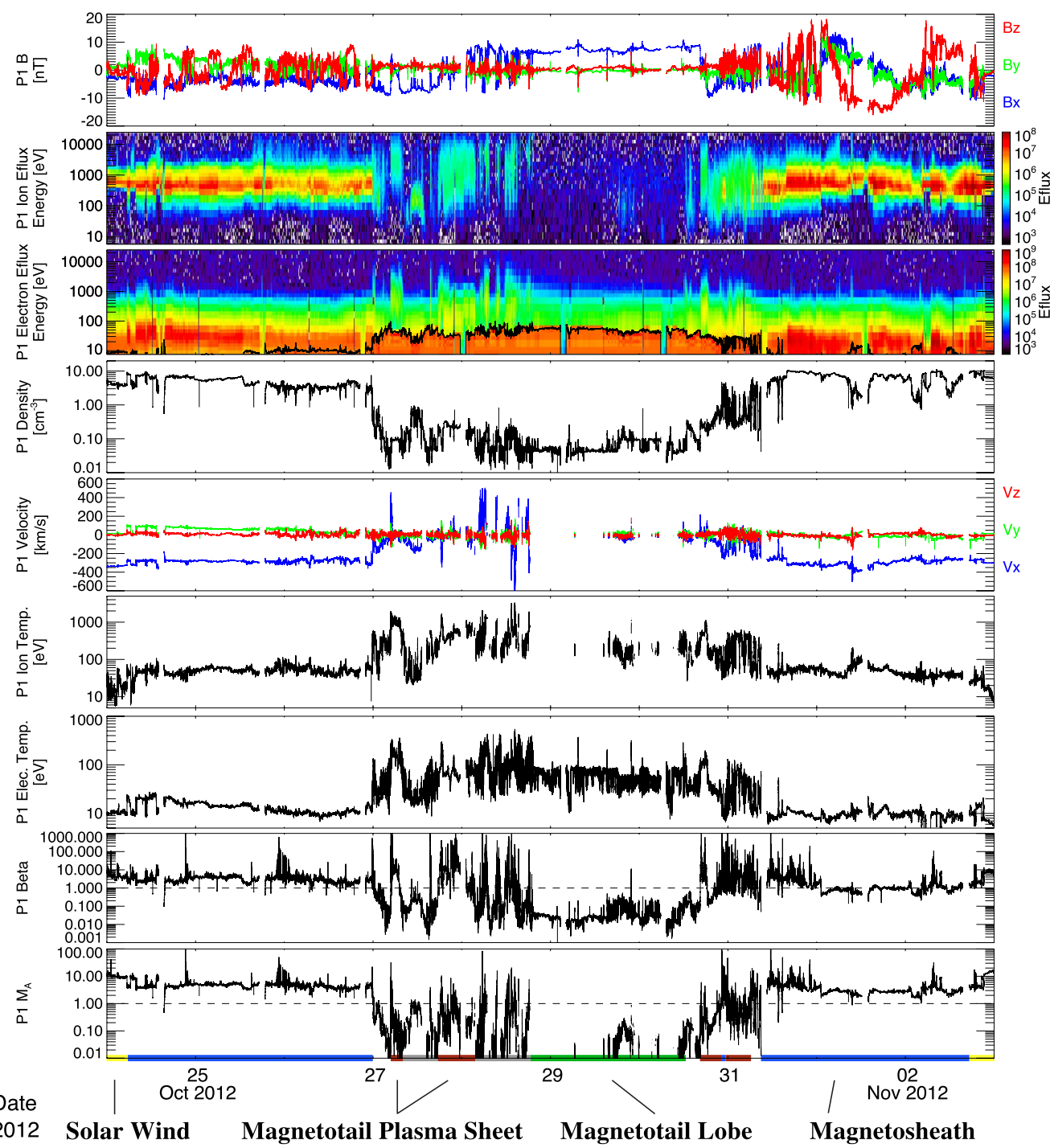


Figure 1. Acceleration, Reconnection, Turbulence, and Electrodynamics of the Moon's Interaction with the Sun P1 observations during a typical passage through Earth's magnetotail between 24 October 2012 and 03 November 2012 (see text for further detail). Colored bars at the bottom illustrate times when the probe was exposed to the (yellow) solar wind plasma, (blue) terrestrial magnetosheath, (red) magnetotail plasma sheet, and (green) magnetotail lobes. Gray bars denote other, more dynamic events (see text).

Besides the solar wind plasma at the edges of the 10-day time period (see yellow bars at the bottom of Figure 1), three distinct, clearly identifiable plasma environments are visible in the ARTEMIS data set. The first environment of note is the terrestrial magnetosheath, detected just after midnight on 24 October 2012 while the P1 probe was exposed to the dusk flank of Earth's magnetosheath. As seen in Figure 1, the ion and electron temperatures

of this shocked plasma reached values of $T_i \approx 40$ eV and $T_e \approx 20$ eV (i.e., warmer than in the solar wind), with a density of $n \approx 4\text{--}8 \text{ cm}^{-3}$ and an anti-Earthward bulk velocity of $\mathbf{V} \approx -250 \text{ km/s}$. The Alfvénic Mach number and plasma beta each exceed a value of 1 within the sheath. ARTEMIS again crossed the terrestrial magnetosheath on the dawn flank just before 12:00 on October 31, during the probe's exit of the magnetotail on the terrestrial dawn side. The blue bars at the bottom of Figure 1 highlight the locations where this sheath plasma was observed during the crossing.

The second region encountered by the probe during this period is the magnetotail plasma sheet, as observed post-midnight on October 27 after crossing the magnetopause. This environment is hotter than the magnetosheath plasma (reaching temperatures of $T_i \gtrsim 1000$ eV and $T_e \gtrsim 100$ eV) but with comparatively reduced velocities, which remained below approximately $|\mathbf{V}| < 100 \text{ km/s}$. Concurrently, the magnetic field was typically lower in magnitude than in the sheath ($|\mathbf{B}| < 5 \text{ nT}$) with all three components close to zero. During the magnetotail crossing, ARTEMIS observed this plasma population multiple times, near 12:00 UT and 18:00 UT on October 27 and from 18:00 UT on October 30 to 08:00 UT on October 31 (see the red bars in Figure 1).

The third notable region detected by the P1 probe during this tail crossing is associated with the Moon's location within the northern lobe of Earth's magnetotail. This extended, quiescent period during which the probe detected the terrestrial magnetotail lobe plasma occurred from approximately 19:00 UT on October 28 to 12:00 UT on October 30 (see the green bar at the bottom of Figure 1). The most striking feature during this time period was the low number density ($n < 0.1 \text{ cm}^{-3}$) associated with only minimal particle fluxes (see the second row of Figure 1). Note that the low (and at times, non-existent) ion fluxes within the magnetotail lobes observed by ARTEMIS make determination of the plasma moments difficult, and sometimes impossible, in the lobes (see also, e.g., Cao, Halekas, Chu, et al., 2020; Liuzzo, Poppe, et al., 2021). The magnetic field during this period was directed almost entirely Earthward, with $B_x > 0$ and a magnitude of $|\mathbf{B}| \approx 10 \text{ nT}$, and the values of β and M_A were well below 1 within this region.

In addition to the magnetosheath, magnetotail plasma sheet, and tail lobe environments, the ARTEMIS data in Figure 1 also show evidence of short and often more dynamic features during the crossing (see the gray bars along the bottom of the figure). For example, near 12:00 UT on October 27, P1 observed an ion population with $n \approx 0.5 \text{ cm}^{-3}$ and a tailward velocity of $V_x \approx -150 \text{ km/s}$, in the presence of generally lobe-like magnetic fields with $B_x < 0$ (indicating the southern tail lobe). This population likely corresponds to the low-latitude boundary layer or, alternatively, the low-latitude plasma mantle (Wang et al., 2014), whereby magnetosheath plasma has entered the magnetotail proper across the magnetopause and continues to convect downstream. Another, more dynamic period of note occurs between 06:00 and 18:00 UT on October 28. Here, ARTEMIS observed a series of high velocity plasma flows ($|\mathbf{V}|$ up to 600 km/s) alternately directed Earthward then tailward, with high temperatures ($T_e \gtrsim 300$ eV and $T_i \gtrsim 1000$ eV) and low densities ($n \lesssim 0.2 \text{ cm}^{-3}$). These high velocity flows are likely ejecta originating from reconnection exhausts in the middle-magnetotail region (e.g., Artemyev, Angelopoulos, Runov, et al., 2017; Kiehas et al., 2018; Runov et al., 2018; Wang et al., 2020). The frequent reversal of flow from Earthward to tailward directions (and vice versa) possibly indicates the repeated movement of the reconnection X-line past the ARTEMIS probes (e.g., Wang et al., 2020) located approximately $60R_E$ downtail.

Figure 1 highlights the various plasma populations to which the Moon is exposed during a typical crossing of the terrestrial magnetotail: flanked by fast flows of the magnetosheath, lobe-like and sheet-like conditions dominate large portions of the plasma environment, with dynamic variability on shorter time scales. However, the rich ARTEMIS data set allows us to perform a statistical analysis of all lunar crossings of the tail over the past 10 years to better characterize the long-term averages of these distinct plasma populations to which the Moon is exposed during nearly a quarter lunation.

3. The Moon in Earth's Magnetotail

We use 126 magnetotail crossings from over 10 years of ARTEMIS observations for this analysis—beginning with the crossing on 08 August 2011 and ending with the crossing on 14 November 2021. For each probe, we define the start of the magnetotail crossing as the probe's final passage through Earth's bow shock on the terrestrial dusk side of the planet, and the end as the first encounter with the bow shock on the dawn side. Although this filters out some observations due to, for example, multiple bow shock crossings during entry into the tail, this ensures that the data set contains only magnetotail plasma. To ensure uniform sampling rates between the P1

and P2 probes, the measurements from each crossing are interpolated to a 4 s cadence. As a whole, this data set comprises more than 50,000 hr of ARTEMIS data that are available to constrain the near-lunar plasma environment within the magnetotail.

In order to separate the different types of plasma regimes to which the Moon is exposed during a terrestrial magnetotail crossing (see, e.g., Figure 1), we establish a set of requirements that categorize the ARTEMIS observations within the magnetotail as either “lobe-like,” “sheet-like,” or “sheath-like.” To categorize the magnetotail plasma into lobe-like and sheet-like conditions, we require that the probe was located within 20° in longitude of the local midnight meridian (i.e., the GSE $-x$ axis) at the time of the measurement. This requirement avoids any bias in sampling between the terrestrial dawn and dusk hemispheres of the magnetotail and prevents magnetosheath plasma from being incorrectly classified as lobe-like or sheet-like. This latter point is consistent with studies by Mieth et al. (2019) and Nguyen et al. (2021) who have shown that ARTEMIS rarely crosses the magnetopause within 20° of the Sun-Earth line near the lunar distance of $\sim 60R_E$ downstream of Earth. Note, however, that this filter does not correct for the magnetotail aberration (e.g., Genceturk Akay et al., 2019), which makes it difficult to completely exclude all of the plasma that is neither lobe-like nor sheet-like from the data set. Using the crossing shown in Figure 1 as an example, P1 was within $\pm 20^\circ$ of the Sun-Earth line from approximately 22:15 on 27 October 2012 through 13:30 on 31 October 2012. Hence, out of nearly 240 hr of data during this crossing, a few hours of magnetosheath plasma is still present even after this filter is applied.

The terrestrial magnetotail lobes are characterized by a magnetic field that mainly points either toward or away from Earth (i.e., the lobe field is predominantly aligned along $\pm \hat{x}$). Hence, to identify lobe-like conditions, we define \mathbf{b}_t to be the moving average of the magnetic field centered over four time windows: $t = 30$ min, $t = 60$ min, $t = 90$ min, and $t = 120$ min. To ensure that the field is predominantly aligned along $\pm \hat{x}$ (i.e., is consistent with the lobes), we require B_x to be the dominant component during each of these windows; that is, $|b_{x,t}| > \psi_t |\mathbf{b}_t|$ for a threshold value of ψ_t . For the moving average over the smallest window, we set the empirically determined threshold parameter to its highest value of $\psi_{30} = 0.93$; that is, within ± 15 min of the measurement, 93% of the field must have been along the $\pm \hat{x}$ direction. This allows for the algorithm to capture rapid transitions from non-lobe-like regions (e.g., within the magnetosheath) into the lobe. However, for the next three windows, the threshold values are slightly reduced to $\psi_{60} = 0.92$, $\psi_{90} = 0.91$, and finally $\psi_{120} = 0.90$. This ensures that the field is sustained along the Earthward/anti-Earthward direction for an extended time and excludes periods where the magnetotail field may happen to be only briefly x -aligned, while still allowing for more gradual transitions into non-lobe-like regions of the magnetotail. In addition to the above, we also require that the value of $|\mathbf{B}|$ at any given point in time is within $\pm 5\%$ of $|\mathbf{b}_t|$ for each of the four time windows. Hence, this approach prevents potentially misidentifying rapid fluctuations in the field as the magnetotail lobes, during time periods that may otherwise be lobe-like (e.g., during the reconnection events detected by ARTEMIS from 06:00–18:00 on October 28; see Figure 1).

Observations within the magnetotail plasma sheet are characterized by a reduction in the magnetic field magnitude (see, e.g., red bars in Figure 1). Hence, to identify sheet-like conditions, we perform separate filtering of the ARTEMIS data, requiring $|b_{30}| < 0.75 |\mathbf{b}_{120}|$. This filter ensures a rapid and sustained drop in the moving average of $|\mathbf{B}|$, such that the 30-min average of magnetic field magnitude is at least 75% lower than the 120-min average. Note that this filter, therefore, excludes encounters with the plasma sheet that may last multiple hours; however, there are still a sufficient number of plasma sheet-like events over the 10-year ARTEMIS mission to obtain reliable statistics for this magnetotail region. Note that while the method defined above is likely not a unique solution to identify lobe- and sheet-like fields, the overall effect of using a different set of persistence filters (e.g., by changing the window sizes used for the moving averages or by setting different threshold values) is only minor on the ten-year-long data set.

Conversely, to reliably identify magnetosheath-like conditions of the magnetotail plasma, we require ARTEMIS to be separated by *at least* 20° longitude from either side of the local midnight meridian, thereby excluding the majority of lobe-like and sheet-like regions. The only additional requirement to be classified as sheath-like is that the plasma number density satisfies $n \geq 1 \text{ cm}^{-3}$, effectively including all boundary layers in the sheath-like classification. Importantly, a given observation may only be classified as either lobe-, sheet-, or sheath-like, but not any combination thereof. Finally, we note that the colored bars presented along the bottom of Figure 1 are not identified using the automated filtering described above.

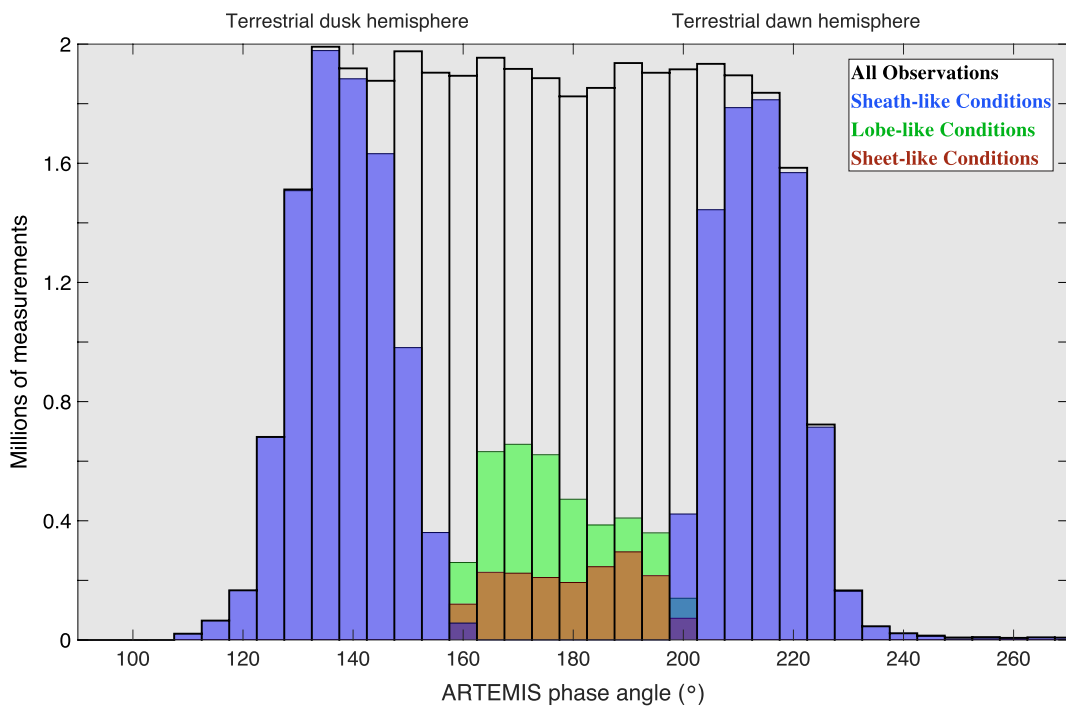


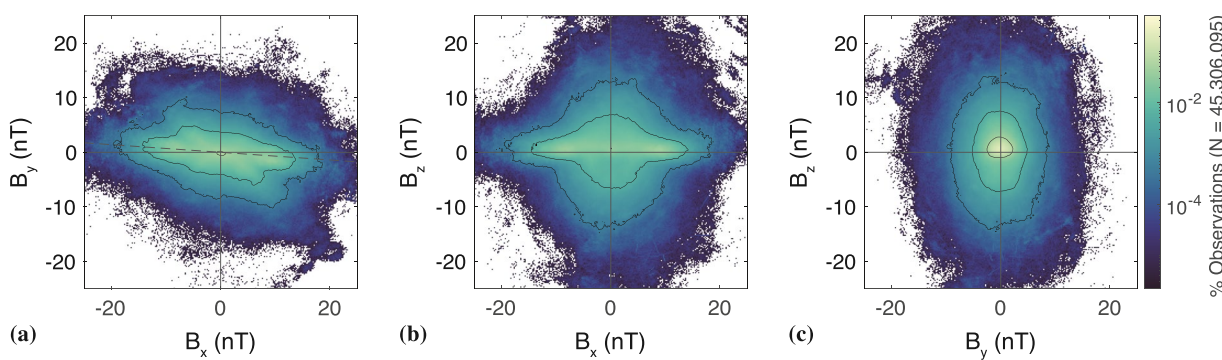
Figure 2. Overlapping histograms of the Acceleration, Reconnection, Turbulence, and Electrodynamics of the Moon's Interaction with the Sun observations within the magnetotail as a function of lunar phase angle separated into 2° bins. Colors correspond to the three magnetotail regions considered in this study: (blue, filled) magnetosheath-like conditions, (green, filled) magnetotail lobe-like conditions, and (red, filled) magnetotail plasma sheet-like conditions. The total number of observations within each bin is indicated by the black outlines.

The distribution of the ARTEMIS observations within the magnetotail as a function of phase angle, and the resulting classifications for the three regions considered in this study, are displayed in Figure 2. Phase increases in a counter-clockwise direction against the Sun-Earth line (i.e., the $+x$ axis of the Geocentric Solar Ecliptic system) as viewed from above the ecliptic plane, such that the terrestrial dusk terminator (the $+y$ axis of GSE) coincides with an angle of 90° , local midnight is located at 180° , and the dawn terminator coincides with 270° . As shown by the black outlines in Figure 2, the distribution of measurements is nearly uniform across all phase angles within the magnetotail (at just under 2 million measurements per bin). However, the aberrated tail structure is apparent, with a shift in the distribution toward dusk (i.e., toward phase angles below 180°), especially visible for magnetosheath-like conditions (filled blue bars in the figure). In addition, Figure 2 illustrates that nearly all observations with the probes separated by more than 20° in longitude from local midnight (i.e., phase angles below 160° and greater than 200°) are classified as magnetosheath-like conditions. Approximately one-quarter of all observations are classified as magnetotail lobe-like (with a slight bias toward dusk; see the filled green bars in the figure), while slightly over one-tenth of observations are classified as sheet-like (with no strong dusk/dawn asymmetry; filled red bars), thereby providing a sufficient number of measurements to accurately characterize these magnetotail regions. The remaining observations within 20° longitude of local midnight do not satisfy the set of filters given above, and are either less representative of the “pure” magnetotail lobes or plasma sheet (including, e.g., magnetosheath encounters within 20° of local midnight or fluctuations in the local environment due to transient plasma events), or are not readily classified as either of these regions (e.g., encounters with the low-latitude boundary layer or plasma mantle; see the regions denoted by the gy bars along the bottom of Figure 1).

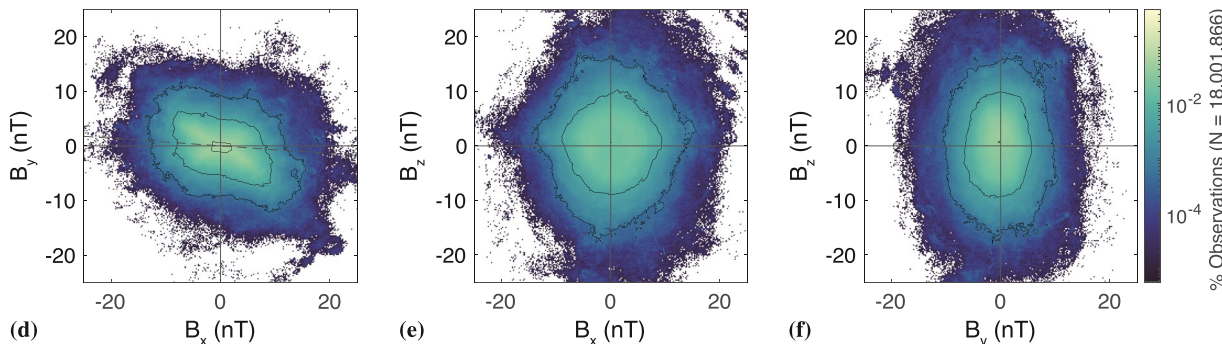
3.1. Properties of the Magnetic Field

Figure 3 displays heatmaps that illustrate the distribution of the magnetic field components observed by ARTEMIS when located within Earth's magnetotail. The top row (panels a–c) includes data from the entire set of magnetotail crossings; that is, from the final bow shock encounter on the terrestrial dusk side to the first encounter on the dawn side for all 126 events. The (a) left, (b) middle, and (c) right columns display the B_x - B_y , B_x - B_z ,

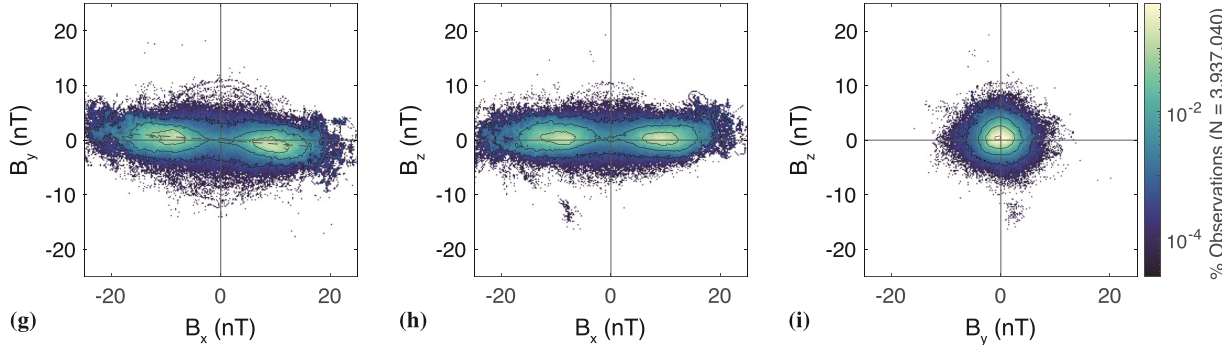
All Observations



Sheath-like Conditions



Lobe-like Conditions



Sheet-like Conditions

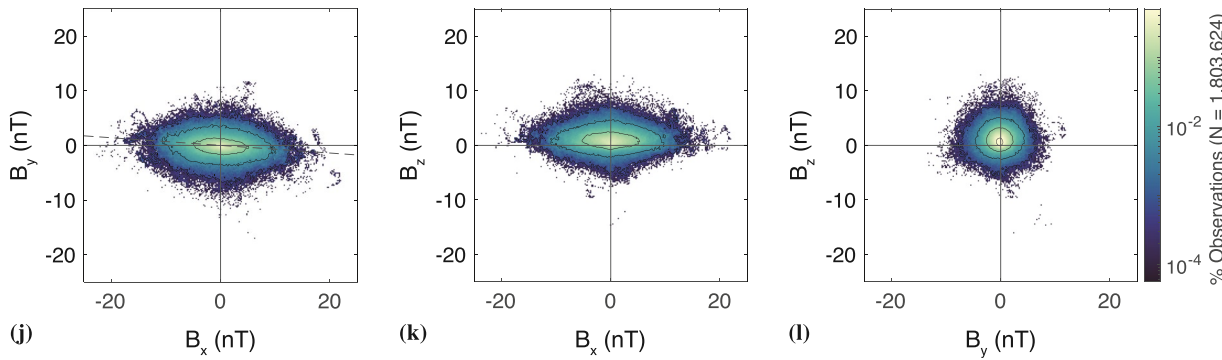


Figure 3. Distributions of the magnetic field components observed by Acceleration, Reconnection, Turbulence, and Electrodynamics of the Moon's Interaction with the Sun when located within Earth's magnetotail for (a–c) all conditions, (d–f) magnetosheath-like conditions only, (g–i) lobe-like conditions only, and (j–l) plasma sheet-like conditions only. Colors correspond to the percentage of total observations N per bin, with N provided at the end of each row. Contours are drawn for each order of magnitude, with the outer-most contour corresponding to a value of $10^{-3}\%$ per bin. Note the differences in color scales and in the number of observations for each row.

and B_y - B_z magnetic field component distributions, respectively, accumulated into linearly-spaced bins with a width and height of 0.2 nT. For each bin, the color scale represents the percentage of time per bin that a given magnetic field component set (e.g., B_x - B_y in panel a) was observed out of the total number of measurements N . For data from all of the crossings presented in the top row of Figure 4, $n = 45, 306, 095$. Contours are included at order-of-magnitude spacing, with the outermost contour corresponding to observations at the $10^{-3}\%$ threshold for each bin. As with the data shown in Figure 1, those times when the probes are located in the Moon's shadow have been removed from the respective data sets to ensure accuracy of the measurements (Georgescu et al., 2011). In addition, we exclude data obtained within $0.5R_M$ of the surface to avoid contaminating the measurements with local perturbations originating from the lunar ionosphere (e.g., Cao, Halekas, Poppe, et al., 2020; Zhou et al., 2013).

To better understand the distinct plasma environments to which the Moon is exposed during a tail crossing, Figure 3 also includes ARTEMIS observations from when the probes were exposed to (d–f) magnetosheath-like, (g–i) magnetotail lobe-like, or (j–l) plasma sheet-like conditions only, after applying the filtering described in the previous section. Note that the total number of observations N is different for each of these environments ($N = 18, 001, 866$ for sheath-like conditions, $N = 3, 937, 040$ for lobe-like conditions, and $N = 1, 803, 624$ for sheet-like conditions).

Panels 3a and 3b show that B_x is broadly distributed within the magnetotail. The largest fraction of observations is centered near $B_x \approx 0$ nT and extends beyond values of ± 10 nT; less frequently, this component reaches $|B_x| > 25$ nT. Panel 3a also highlights a slight asymmetry in B_y with respect to B_x , especially visible beyond $|B_x| \approx 10$ nT. This effect is due to the aberration of the terrestrial magnetosphere (see also, e.g., Behannon, 1970; Kaymaz et al., 1994; Mihalov et al., 1968), whereby Earth's orbital velocity causes the down-tail magnetosphere to be tilted in the orbital plane against the Sun-Earth line by approximately 4° , although deviations beyond 20° have been observed resulting from non-radial components to the solar wind flow (Gencturk Akay et al., 2019). To guide the eye and more clearly illustrate this effect, panel 3a includes a dashed line that is tilted at an angle of 4° against the $B_y = 0$ line, which closely follows this asymmetry in the magnetic field components.

An additional feature of the magnetic field distribution within the magnetotail is a positive offset to the B_z component. Panels 3b and 3c show that B_z preferentially reaches values between $-1 \text{ nT} \leq B_z \leq 4 \text{ nT}$, centered around $B_z \approx +1$ nT. In addition to these ten-year-long ARTEMIS observations, a similar signature of the positive B_z offset near the Moon has been observed (over shorter timescales) by the ISEE-3 spacecraft (e.g., Slavin et al., 1985; Zwickl et al., 1984), as well as by the Lunar Prospector and Kaguya missions (see Mittelholz et al., 2021). This positive bias in B_z is a signature of the orientation of Earth's magnetic dipole, which has a $B_z > 0$ component near the lunar orbit, and is visible for each of the three magnetotail conditions in this study (see Figure 3).

Panels 3b and 3c show that while B_z remains mostly within ± 10 nT, this component at times extends beyond ± 20 nT. This is most clearly visible at times when B_x and B_y are minimized, where the north/south component reaches values beyond $|B_z| > 20$ nT. These tails—approaching large values in the B_z distribution—are indicative of the behavior of the magnetic field within the magnetosheath. The draping of the interplanetary magnetic field preferentially imparts a z -component to the magnetic field orientation (e.g., Behannon, 1968; Sibeck et al., 1986). This becomes especially clear in panels 3e and 3f, which show the magnetic field for magnetosheath-like conditions alone. In panel 3d, the two inner-most contours—representing the most frequently observed set of magnetic field conditions—are more strongly tilted than the dashed line corresponding to a tail aberration angle of 4° . Rather, B_y is tilted by an angle of nearly 45° against the B_x component, consistent with the angle of the Parker spiral near Earth's orbit.

The number of ARTEMIS measurements within the magnetotail lobes shown in panels 3g–3i is reduced by more than a factor of 10 compared to the total number of points obtained during the full data set. Here, the distributions illustrate that the magnetic field is mainly aligned with $\pm \hat{x}$ (as is expected given our filter identifying lobe-like conditions), reaching a value of $B_x \approx \pm 10$ nT for a large fraction of the time spent within the lobes. This field strength is approximately 33% lower than the magnitude of the B_x component observed during the early stages of the ISEE-3 mission: using 4 months of data from the spacecraft's initial magnetotail passes, Slavin et al. (1985) found that the magnitude of the terrestrial lobe field follows a power-law decrease with increasing distance downstream of Earth, reaching $|\mathbf{B}| \approx 15$ nT near $-60R_E$. Although the ISEE-3 measurements were obtained during solar maximum (just after its peak), the strength of the lobe field observed by ARTEMIS does not display a strong

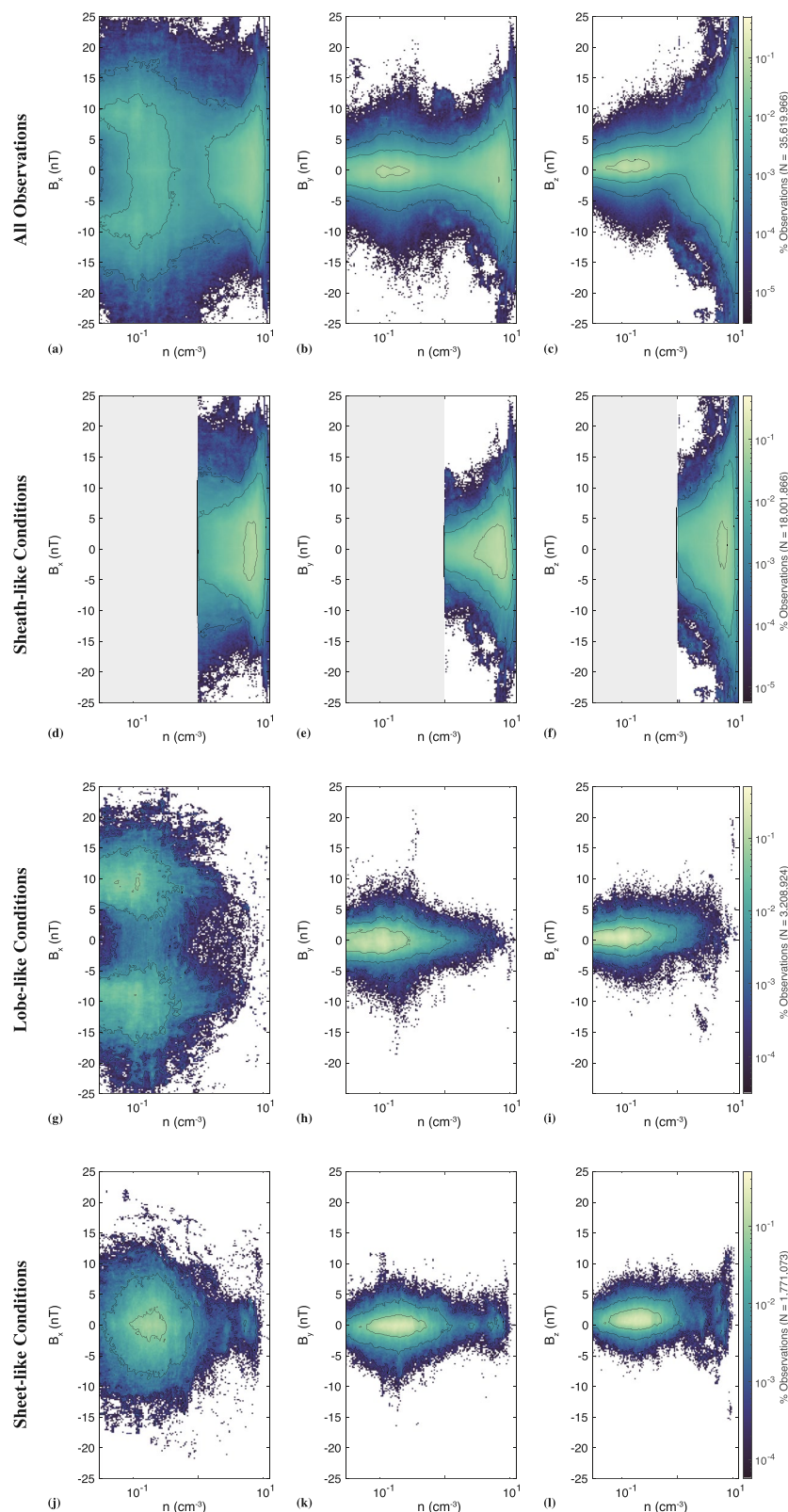


Figure 4. Heatmaps displaying magnetic field components as a function of electron number density for the same magnetotail conditions as displayed in Figure 3. Instrument counts corresponding to densities below 0.03 cm^{-3} are excluded to ensure an accurate density calculation.

dependence on the most recent solar cycle. As with the full set of observations, the aberration of the magnetotail is clearly visible in panel 3g, where B_y in the lobes is tilted by approximately 4° (see dashed line in the panel). The spread of B_y and B_z is now much narrower within the lobes, distributed nearly isotropically around 0 nT (see panel 3i). Here, the peak in lobe-like observations occur with $B_y = -1$ nT and $B_z = +1$ nT, with a limited number of measurements occurring while B_y or B_z exceeds ± 5 nT. Over the entire 10-year period, more than 99.99% of all observations with lobe-like fields satisfy -10 nT $\leq B_y, B_z \leq 10$ nT.

For the sheet-like conditions displayed in panels 3j–3l, the strength of the field drops by a factor of nearly 3, from an average value of $|\mathbf{B}| \approx 10$ nT in the lobes to a value of $|\mathbf{B}| < 4$ nT in the sheet. This is mainly driven by the lack of a strong x -aligned field component near the center of the plasma sheet, although each component of the magnetic field is more focused near a value of ~ 0 nT. Few ARTEMIS observations of $|B_y|$ or $|B_z|$ in the sheet exceed a value of 10 nT, while B_x rarely (less than $\sim 0.001\%$ of the time per each bin) falls outside the range of -10 nT $\leq B_x \leq +10$ nT. The positive offset in the north/south component of the field is still apparent within the central plasma sheet, as is the aberration of the magnetotail, albeit to a lesser amount within the sheet compared to within the lobes (cf. panels 3g and 3j).

Figure 4 displays the distribution of the magnetic field components within the magnetotail measured by ARTEMIS as a function of electron number density for the same conditions as in Figure 3; that is, (a–c) all observations, (d–f) sheath-like conditions, (g–i) lobe-like conditions, and (j–l) sheet-like conditions. For these, we do not include measurements of densities below $n < 0.03 \text{ cm}^{-3}$, to ensure accurate calculations of the ion moments which become unreliable when ARTEMIS detects too few geophysical particle counts (McFadden, Carlson, Larson, Bonnell, et al., 2008; Poppe, 2019); recall that this is automatically satisfied for sheath-like conditions since we require $n \geq 1 \text{ cm}^{-3}$. Note that a population of even lower-density plasma may at times be present within the lobes of the magnetotail that is “hidden” from the ARTEMIS probes when exposed to sunlight (see Liuzzo, Poppe, et al., 2021), the effect of which is not included in this analysis. Due to this additional requirement on the plasma density, the number of observations used to generate the heatmaps in each row of Figure 4 is reduced compared to Figure 3 by as much as 21%.

The top row of Figure 4 highlights a distinct correlation between the density and magnetic field components. Within the magnetotail, Panels 4b and 4c show that the ambient magnetospheric density near the lunar orbit is most frequently centered near a value of $n \approx 0.2 \text{ cm}^{-3}$, correlated with minima in $|B_y|$ and $|B_z|$. For nearly all observations with densities $n \lesssim 0.2 \text{ cm}^{-3}$, B_y and B_z remain within approximately ± 15 nT. For the B_x component, the peak in ARTEMIS observations near a density of $n \approx 0.2 \text{ cm}^{-3}$ is much more extended compared to the other two components, nearly evenly distributed for all values within $|B_x| \lesssim 10$ nT. With increasing densities, however, the magnitudes of each field component extend to successively larger values. At densities beyond $n \gtrsim 1 \text{ cm}^{-3}$, all three components reach values up to approximately ± 15 nT at a frequency that is nearly evenly distributed, with $|B_x|$ and $|B_z|$ reaching maxima beyond 25 nT. This feature marks the ARTEMIS probes' encounters with the edge of the terrestrial magnetosheath: as also visible in Figures 4d–4f, the densities for sheath-like conditions peak near a value of 8 cm^{-3} with a broad spread in each component of the magnetic field (see also Figures 3d–3f).

Figures 4g–4i further confirm that the higher-density plasma is associated with the lunar passage through the magnetosheath: the ambient plasma density within the lobes of the terrestrial magnetotail near the lunar orbit rarely exceeds a value of 1 cm^{-3} . Rather, the contour denoting the most frequent observations illustrates that the tenuous lobe-like plasma reaches densities as low as $n = 0.03 \text{ cm}^{-3}$ (i.e., the ARTEMIS ESA detection limit considered for this study) and extends to values an order of magnitude larger with $n \approx 0.3 \text{ cm}^{-3}$. The structure of the magnetic field within the lobes is also clearly visible in panels 4g–4i. In B_x , a bifurcated signature forms near a density of $n = 0.1 \text{ cm}^{-3}$, with the maxima in observations centered near $B_x = \pm 10$ nT. Conversely, the B_y and B_z components remain near a value of 0 nT, with the largest number of observations between $-2 \text{ nT} < B_y, B_z < 2 \text{ nT}$; nearly every lobe-like measurement of these components remained within ± 10 nT over the course of the 10-year data set.

For sheet-like conditions, Figures 4j–4l illustrate that the densities observed by ARTEMIS are, on average, shifted to slightly larger values than in the magnetotail lobes: the inner-most contour in each panel now encompasses values from $0.08 \text{ cm}^{-3} < n < 0.7 \text{ cm}^{-3}$, nearly three times higher than in the lobes. As also seen in Figures 3j–3l, the magnetic field within the sheet is reduced in magnitude, with B_x and B_y centered around 0 nT and an overall positive shift in B_z (see also Behannon, 1970).

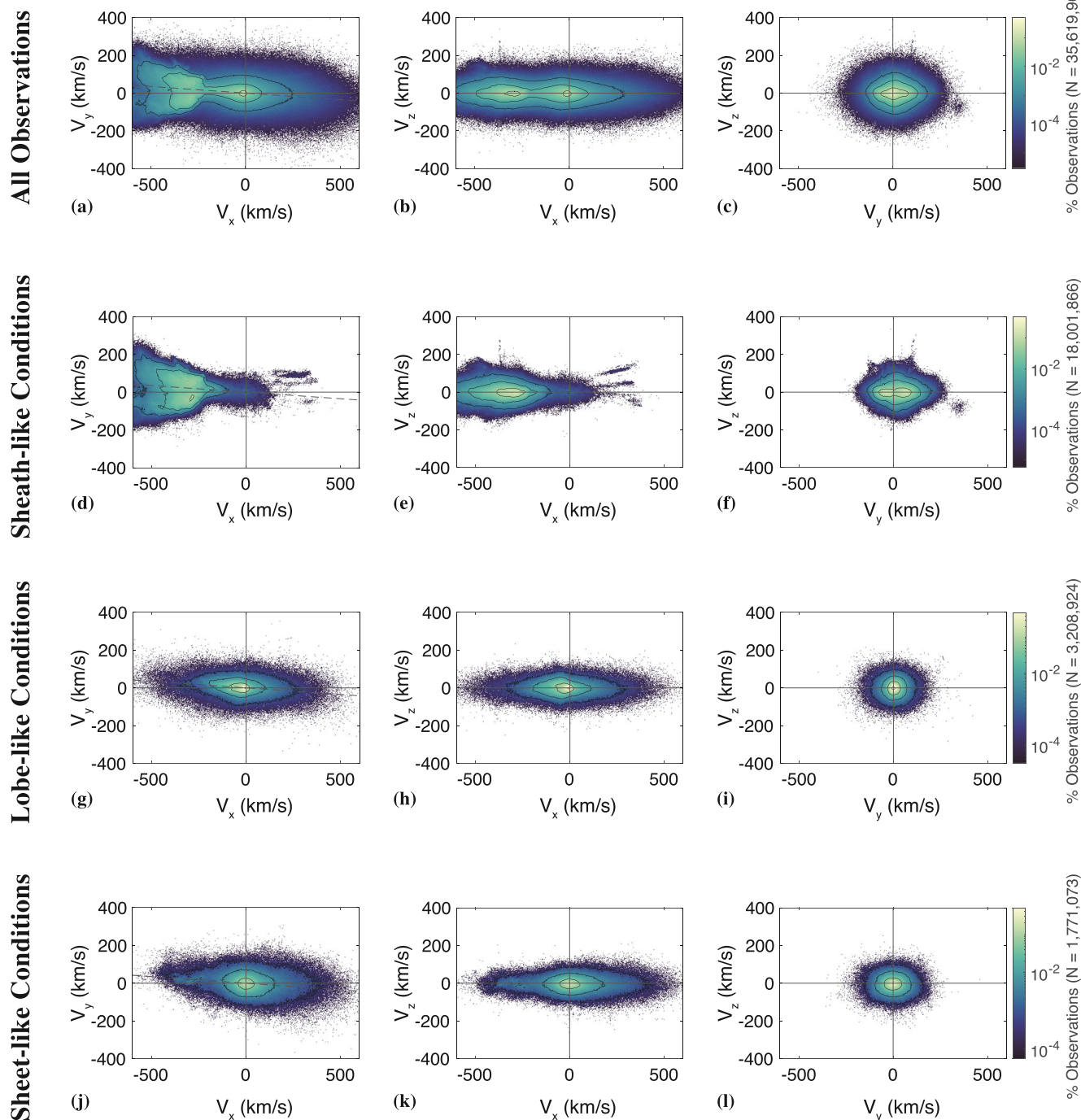


Figure 5. Identical to Figure 3, but for the components of the bulk plasma velocity. Note that velocities calculated using instrument counts that correspond to number densities of $n < 0.03 \text{ cm}^{-3}$ are excluded from the data set.

3.2. Properties of the Plasma Velocity

Figure 5 displays heatmaps for the ARTEMIS measurements of the bulk plasma velocity components within the terrestrial magnetotail, in the same layout as Figure 3. The top row (5a–5c) includes all 10 years of observations, whereas the lower three rows separate the data into (5d–5f) magnetosheath-like, (5g–5i) magnetotail lobe-like, and (5j–5l) sheet-like conditions, respectively. To ensure accuracy in the velocity moment, we only calculate velocities using instrument counts that correspond to number densities of $n > 0.03 \text{ cm}^{-3}$ in Figure 5 (as also

consistent with Figure 4). The observations of the velocity components are accumulated into linearly-spaced bins with a width and height of approximately 3 km/s.

Figures 5a and 5b highlight that the V_x component of the flow is shifted noticeably tailward (i.e., $V_x < 0$), with a median value of $V_x = -240$ km/s. The distribution of V_x in the magnetotail is bimodal, with the most frequent observations peaking near values of $V_x \approx 0$ km/s and $V_x \approx -400$ km/s. For the former, the V_y component of the bulk plasma velocity remains near a value of ~ 0 km/s, with speeds that only rarely extend beyond 100 km/s. For the latter, however, V_y displays a distinct divergence to large velocities for the most negative values of V_x (i.e., for the fastest tailward flows), frequently reaching speeds approaching $|V_y| \approx 200$ km/s. The V_z component of the magnetotail flow, on the other hand, displays only a narrow, symmetric spread about its mean value of $V_z \approx 0$ km/s and rarely exceeds 200 km/s, with most commonly observed velocities of $|V_z| \lesssim 25$ km/s.

Figures 5d–5f illustrate that the divergent behavior in V_y is driven by the flow within the terrestrial magnetosheath. After encountering the Earth's magnetic field, shocked solar wind plasma is diverted and imparts a strong component to the flow directed away from the planet (resulting in a $\pm V_y$). The signature of the aberrated tail is also visible, with the V_y component symmetric about the dashed line in panel 5 corresponding to a 4° tilt. These panels also show that the magnetosheath flows are almost entirely tailward, with a mean value of V_x exceeding -300 km/s. Note that the limited observations suggesting $V_x > 0$ velocities (for less than 0.001% per bin; see panels 5d and 5e) may satisfy the requirements for sheath-like conditions described above but are likely *not* associated with Earthward magnetosheath flows.

For lobe-like conditions, Figures 5g–5i show that each velocity component is more narrowly distributed compared to the whole data set. In V_y and V_z , nearly all observations occur with -100 km/s $< V_y, V_z < +100$ km/s. Panel 5i illustrates that these components are nearly isotropic, and were most frequently observed (at more than 1% of the time per bin) between values of -9 km/s $< V_y < +6$ km/s and -9 km/s $< V_z < +3$ km/s. ARTEMIS detected V_x flows that were most frequently shifted anti-Earthward (i.e., $V_x < 0$) within the lobes, with the peak in measurements located between -100 km/s $< V_x < 20$ km/s (see panel 5g). Despite this tailward offset at lower velocities, the distribution for cases with $|V_x| \gtrsim 250$ km/s is remarkably symmetric (see Figures 5g and 5h), with considerable Earthward *and* anti-Earthward flows for these lobe-like conditions. These somewhat frequent, high-velocity measurements are likely signatures of reconnection events within the tail: the Earthward velocities suggest a translunar X-line well down-tail of the ARTEMIS probes (e.g., Kiehas et al., 2018; Slavin et al., 1985), while the anti-Earthward velocities—suggesting cislunar reconnection—emphasize the variability in the location of the tail reconnection region. As a result, these signatures frequently pass ARTEMIS located near $60R_E$ downstream of the planet, resulting in both Earthward and tailward velocities being observed by the probes (see also Figure 1 and Artemyev, Angelopoulos, Runov, et al., 2017; Wang et al., 2020).

For plasma sheet-like conditions, the bottom row of Figure 5 still illustrates a broad spread in V_x at velocities exceeding $|V_x| > 250$ km/s, likely signatures of magnetotail reconnection events. However, all three components were more commonly observed at lower values: the most frequent measurements were obtained with -50 km/s $< V_x, V_y, V_z < 50$ km/s. Hence, compared to flows within the magnetotail lobes, the peak in the distribution of the velocity components observed within the plasma sheet is more symmetric around 0 km/s, especially along the x direction.

Figure 6 displays the components of the plasma bulk velocity as a function of electron number density as observed by ARTEMIS within the magnetotail, following the layout of the previous three figures. As with the magnetic field (see Figure 4), there is a distinct correlation between the flow velocity and number density. For the whole set of observations (panels 6a–6c), each velocity component has two separate regions corresponding to peaks in the observations. One of these is located at low densities centered near $n \approx 0.1 \text{ cm}^{-3}$, with panels 6b and 6c showing that the most frequent observations occurred with $0.03 \text{ cm}^{-3} < n < 0.5 \text{ cm}^{-3}$. As also visible in Figure 5, this peak spans a broad range of V_x values extending beyond $|V_x| \gtrsim 300$ km/s, but is narrower in V_y and V_z . The second enhancement is located at higher densities ($n > 5 \text{ cm}^{-3}$), centered near a value of $n \approx 8 \text{ cm}^{-3}$. Notably, this high-density enhancement is associated with strong tailward velocities of $V_x \approx -300$ km/s (see panel 6a) and a bifurcation in V_y . As visible in panels 6d–6f, this second peak is indicative of the probes' passage through the magnetosheath plasma (see also Figure 5).

Comparing the bottom two rows of Figure 6 highlights the differences between the plasma environment within the magnetotail lobes and plasma sheet. Specifically, lobe-like conditions are, most frequently, associated with

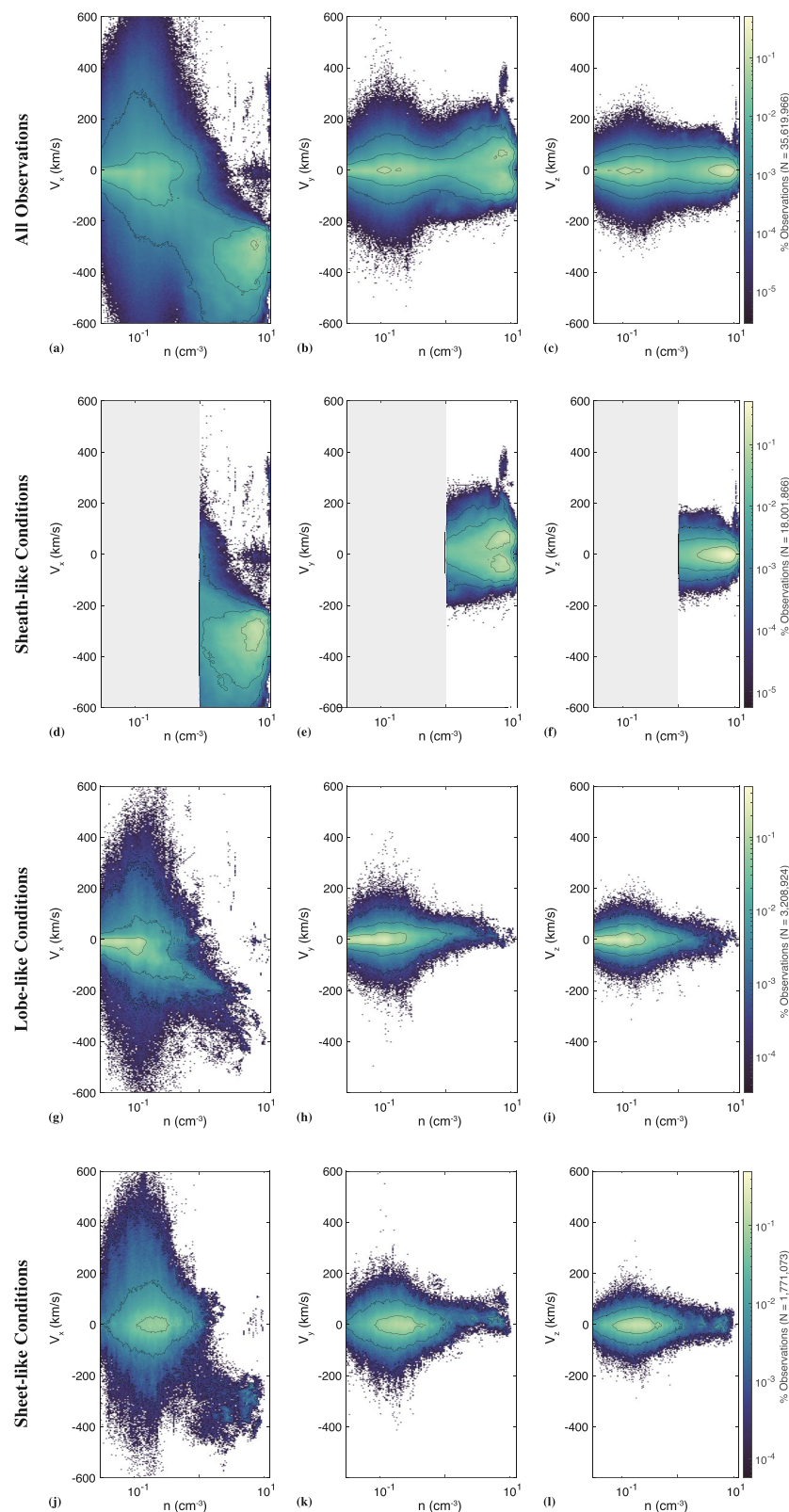


Figure 6. Identical to Figure 4, but for the components of the plasma bulk velocity as a function of number density.

a more tenuous plasma with $n \lesssim 0.2 \text{ cm}^{-3}$, while sheet-like conditions are associated with a denser plasma with $n \gtrsim 0.2 \text{ cm}^{-3}$ (cf. panels 6g–6i with panels 6j–6l). Note that despite the filtering for lobe-like and sheet-like conditions, a small amount of magnetosheath-like plasma ($\lesssim 0.01\%$ per bin) is still present for these regions, especially visible at high densities ($n > 1 \text{ cm}^{-3}$) and strong tailward velocities ($V_x \ll 0$). As also seen in Figure 5, panel 6g illustrates that the signature of reconnection outflow is visible in the data even for lobe-like conditions, with Earthward and tailward velocities reaching $|V_x| \approx 500 \text{ km/s}$.

While similar high-velocity flows are also present in panel 6j for magnetotail plasma sheet-like fields (see also Figure 5), they are more often directed Earthward (with flows reaching values up to $V_x = +600 \text{ km/s}$) than they are tailward (with flows that rarely exceed $V_x = -400 \text{ km/s}$). This may suggest reconnection regions within the plasma sheet that are more frequently located tailward of the Moon. Such a finding is consistent with Slavin et al. (1985), who found that the location of the down-tail reconnection region was on average located $120R_E$ – $140R_E$ downstream of the Earth during the ISEE-3 magnetotail encounters. This result also agrees with the study by Kiehas et al. (2018), who used data from the first 5 years of the ARTEMIS mission and found that a large fraction (43%–56%) of the reconnection-related flows detected within the magnetotail plasma sheet were directed Earthward. However, the large spread in V_x visible in Figure 6j—reaching large values both Earthward and tailward—again suggests a highly variable location to the neutral line (see also Kiehas et al., 2018).

3.3. Statistics of the Lunar Plasma Environment Within the Magnetotail

Figure 7 displays overlapping histograms of (7a) components of the magnetic field, (7b) components of the bulk plasma velocity, and (7c) plasma number density, ion temperature, ion and electron temperature ratio, and ion-specific entropy for the same four scenarios in the previous figures: (black, outlined) all ARTEMIS observations within the magnetotail, (blue, filled) magnetosheath-like conditions, (green, filled) magnetotail lobe-like conditions, and (red, filled) plasma sheet-like conditions. Here, the ion-specific entropy s_i is proportional to the ratio between the ion plasma pressure p_i and the number density ($s_i \propto p_i/n_i^\gamma$; see, e.g., Borovsky et al., 1998; Goertz & Baumjohann, 1991; Wing et al., 2014). For each of the conditions, we assume that the plasma is isotropic with a polytropic index $\gamma = 5/3$ for simplicity (e.g., Baumjohann, 1993). The histograms in Figure 7 are normalized by the total number of observations for each respective scenario (i.e., the values of N as provided in Figure 3 for the magnetic field or in Figure 5 for the plasma moments). Again, note that for measurements of the plasma moments in panels 7b and 7c, we require sufficient ARTEMIS instrument counts corresponding to an ambient density of $n > 0.03 \text{ cm}^{-3}$. The magnetic field histograms in panel 7a are accumulated into bins that are 2 nT wide, panel 7b uses a 20 km/s bin width for the velocity, and the bins for temperature in panel 7c are 25 eV wide. The bin widths for the number density, temperature ratio, and entropy each increase logarithmically: for density, the bins increase from a width of $4.26 \cdot 10^{-3} \text{ cm}^{-3}$ at the lowest densities to a bin width of 2.49 cm^{-3} at the highest densities, for the temperature ratio, the bins increase from widths of 0.05 to 4.50, and for specific entropy, the bins increase from $1.27 \cdot 10^{-4} \text{ nPa cm}^5$ in width to 0.84 nPa cm^5 . Besides the normalized histograms, each panel in Figure 7 includes the median value for each quantity, represented by vertical dashed lines, as well as the standard deviation above and below the median, represented by horizontal lines along the top of each panel. Additional statistical parameters for these quantities can be found in Table 1.

Figure 7a shows that the B_y and B_z components of the magnetic field within the magnetotail lobes and plasma sheet are similar, peaking near 0 nT for each of the separate regions that rapidly decrease at larger magnitudes. Notably, the histogram for B_z is clearly shifted toward positive values for each of the magnetotail locations, with the median value near the central plasma sheet (0.97 nT) nearly a factor of two larger than in the lobes (0.51 nT). Again, this overall shift of $B_z > 0$ is indicative of the orientation of the magnetospheric field near the lunar orbit (as is also visible in, e.g., Figure 3 and Table 1). Within the magnetosheath, the B_y and B_z components are similarly centered near zero (with a slightly positive shift in B_z), but their distributions are much broader compared to within the lobes or plasma sheet.

Despite similarities in B_y and B_z for magnetotail lobe-like and sheet-like conditions, the differences in the field configurations for these two scenarios become visible in B_x and $|\mathbf{B}|$. In B_x , the histograms for the northern and southern lobes are bimodal, nearly following two normal distributions centered around $\pm 10 \text{ nT}$, with standard deviations of nearly 3 nT. Within the sheet, while the spread of B_x is similar as in each of the lobes, the distribution is much more focused near $B_x \approx 0 \text{ nT}$ than in the lobes. The magnetosheath field is also nearly centered around 0 nT, but with a distribution that is again much broader than that of the sheet-like fields. The magnetic

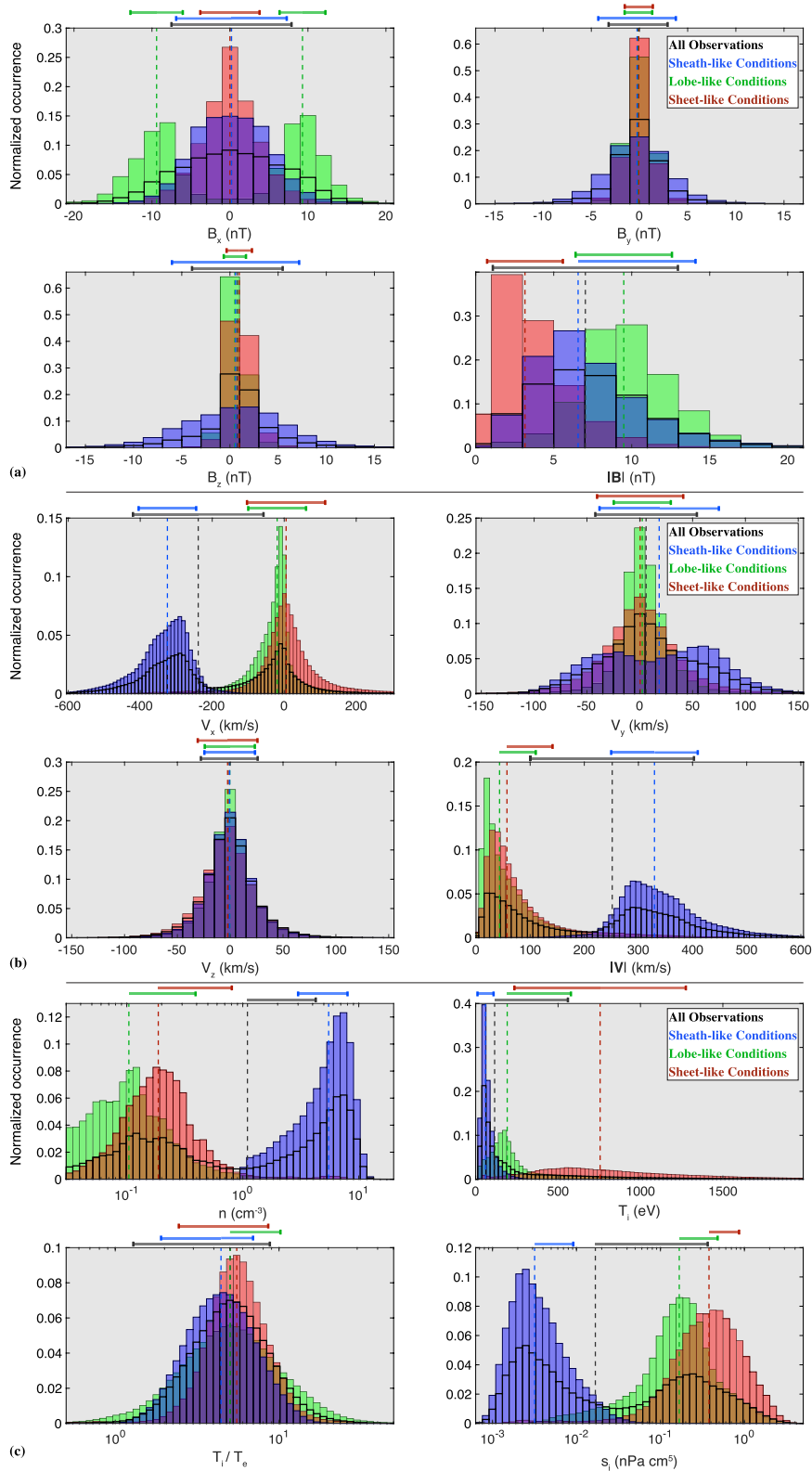


Figure 7.

field magnitude is noticeably different between each of these magnetotail regions as well. The median value of $|\mathbf{B}| = 3.16$ nT is at its smallest within the plasma sheet and is more than two times lower than the median within the magnetosheath of $|\mathbf{B}| = 6.53$ nT, which itself is nearly 1.5 times lower than the median value of $|\mathbf{B}| = 9.48$ nT within the magnetotail lobes. The weakened field magnitude within the plasma sheet is a characteristic feature of the magnetotail, coinciding with the passage through the neutral region of the magnetotail field (e.g., Bame et al., 1967).

Figure 7b shows the velocity distribution; for lobe- and sheet-like conditions (green and red, respectively, in Figure 7b), the V_x components are approximately symmetric about $V_x = 0$ km/s. However, the distribution is shifted tailward for lobe-like conditions (with a median value of $V_x = -20$ km/s), while the sheet-like distribution is shifted slightly Earthward (with a median of $V_x = +4$ km/s). In comparison, the magnetosheath flow is decidedly tailward, with a median value of $V_x = -324$ km/s and tailward speeds that only rarely drop below 200 km/s. In V_y , the lobe-like and sheet-like distributions are similar, nearly symmetric around $V_y = 0$ km/s, with the distribution of the lobe-like flows more narrowly peaked than for sheet-like conditions. The deflected plasma flow within the magnetosheath is especially visible in this figure, with a bimodal distribution in V_y consisting of peaks located near -30 km/s and $+60$ km/s (i.e., slightly biased toward the $+\hat{\mathbf{y}}$ direction). Notably, measurements with $V_y > +100$ km/s (i.e., within the dusk flank of the magnetosheath) occur more frequently than those with $V_y < -100$ km/s (i.e., within the dawn flank). These asymmetries are signatures of the aberration in the magnetotail at the lunar orbit, as was also visible in Figure 5d. The distribution of the V_z component is nearly independent of the location of the probes within the magnetotail; instead, the north/south component of the flow always follows a quasi-normal distribution that is centered near $V_z = 0$ km/s.

Figure 7c shows normalized histograms for the electron number density and plasma temperature in the magnetotail. As also visible in Figures 4 and 6, the densities are, on average, lower in the lobes than the plasma sheet, with a slight overlap near a value of $n \approx 0.2$ cm $^{-3}$. These, however, are each dwarfed by the densities within the magnetosheath which peak at over an order of magnitude larger, near values of $n \approx 8$ cm $^{-3}$. Panel 7c illustrates a stark difference in the plasma temperatures for these separate magnetotail plasma conditions as well, with the coldest population within the magnetosheath (with median temperatures of $T_e = 14$ eV and $T_i = 60$ eV), followed by the warmer magnetotail lobes (with medians of $T_e = 39$ eV and $T_i = 190$ eV) compared to the warmest plasma within the sheet (with medians $T_e = 132$ eV and $T_i = 733$ eV). For this warmest population, the distribution has a long tail that extends to temperatures beyond 2,000 eV within the sheet. Using the average values for number density, temperature, and magnetic field strength in Table 1, we find that the magnetotail lobe-like conditions are in pressure balance with the plasma sheet-like conditions to within $\sim 10\%$ (see also Matsumoto et al., 2001). This minor difference may be due to the presence of particles within the plasma sheet that exceed the energy range observable by the ARTEMIS Solid State Telescope (e.g., Angelopoulos, 2008; Sarris et al., 1981).

Figure 7 also illustrates that the mean value for the ratio between the ion and electron temperatures is near 5 for all scenarios studied (see also Table 1). The distribution of this ratio for lobe-like conditions (with median value $T_i/T_e = 5.52$) is narrower than those of the sheath-like (median $T_i/T_e = 4.96$) or lobe-like populations (median $T_i/T_e = 5.02$). The average values for the ion and electron temperature ratios near the lunar distance of $60R_E$ are consistent with the measurements within the near-Earth magnetotail (see, e.g., Grigorenko et al., 2016; Lavraud et al., 2009; Wang et al., 2012; Wing et al., 2014). However, the ARTEMIS observations reach values that extend beyond the range of T_i/T_e observed closer to Earth—especially within the lobes where T_i/T_e even drops below 1. Also visible in Figure 7 is a clear separation in the specific entropy of the ions. As is the case closer to Earth (see, e.g., Wing et al., 2014), s_i within the magnetosheath is, on average, 2–3 orders of magnitude below the value within the magnetotail plasma sheet near the Moon's orbital position. For lobe-like conditions, the ion-specific entropy is (on average) slightly reduced compared to the plasma sheet, but at times reaches values similar to those observed within the magnetosheath due to the substantial spread of the entropy distribution.

Figure 7. Overlapping histograms of the (a) magnetic field (b) bulk plasma velocity, and (c) plasma number density, ion temperature, ion and electron temperature ratio, and ion-specific entropy as observed by Acceleration, Reconnection, Turbulence, and Electrodynamics of the Moon's Interaction with the Sun for (black, outlined) all conditions, (blue, filled) magnetosheath-like conditions only, (green, filled) lobe-like conditions only, and (red, filled) plasma sheet-like conditions only. Each panel is normalized by the number of observations for the respective magnetotail condition. For each condition, dashed vertical lines represent the median value of the respective quantity, while horizontal bars at the top of each panel denote the standard deviation, centered at the median value (see Table 1 for relevant parameters). Note that standard deviations below the median value are not included for cases that would result in a negative magnitude, density, temperature, or entropy.

Table 1

Statistical Parameters for the Magnetic Field, Plasma Flow Velocity, Number Density, Ion and Electron Temperature, Ion and Electron Temperature Ratio, and Ion Specific Entropy With the Moon Located Within Earth's Magnetotail

Magnetic field (nT)	σ	μ	Me	Mo	K	Sk
B_x : All	6.73	0.17	0.20	0	2.56	-0.05
B_x : Sheath-like	4.81	0.27	0.19	0	3.22	0.12
B_x : Lobe-like (N)	2.90	9.33	9.30	9	4.02	0.00
B_x : Lobe-like (S)	3.17	-9.66	-9.38	-9	3.70	-0.17
B_x : Sheet-like	3.79	-0.05	0.00	0	4.08	-0.05
B_y : All	2.67	-0.17	-0.14	0	6.18	-0.10
B_y : Sheath-like	3.41	-0.25	-0.25	0	4.30	-0.05
B_y : Lobe-like	1.43	-0.08	-0.11	0	7.26	-0.04
B_y : Sheet-like	1.46	-0.08	-0.07	0	7.46	-0.21
B_z : All	3.81	0.65	0.77	1	5.78	-0.31
B_z : Sheath-like	5.28	0.37	0.58	1	3.18	-0.10
B_z : Lobe-like	1.15	0.56	0.51	0	10.6	0.12
B_z : Sheet-like	1.32	1.08	0.97	1	8.21	0.47
$ B $: All	3.63	7.35	7.00	6	3.30	0.61
$ B $: Sheath-like	3.46	7.12	6.53	6	4.02	0.94
$ B $: Lobe-like	2.95	9.70	9.48	9	3.72	0.27
$ B $: Sheet-like	2.41	3.68	3.16	2	5.64	1.34
Velocity (km/s)	σ	μ	Me	Mo	K	Sk
V_x : All	175	-189	-240	-8	1.97	0.12
V_x : Sheath-like	77.6	-335	-324	-288	5.29	-0.28
V_x : Lobe-like	73.1	-30.0	-19.8	-7	10.6	-0.83
V_x : Sheet-like	95.2	3.99	4.15	-1	7.40	-0.82
V_y : All	46.1	9.28	5.83	0	3.14	0.14
V_y : Sheath-like	55.1	15.2	17.9	63	2.18	-0.04
V_y : Lobe-like	25.1	3.69	2.37	1	8.09	0.06
V_y : Sheet-like	37.9	0.67	0.37	0	4.49	0.04
V_z : All	26.4	-0.81	-0.90	-1	5.76	0.06
V_z : Sheath-like	23.8	-0.13	-0.50	-1	5.64	0.20
V_z : Lobe-like	23.2	-0.21	-0.40	0	6.73	0.00
V_z : Sheet-like	27.7	-2.84	-2.46	-1	5.41	-0.03
$ V $: All	149	218	251	23	1.81	0.14
$ V $: Sheath-like	77.1	340	329	293	4.06	0.52
$ V $: Lobe-like	64.2	63.9	43.4	18	14.7	2.82
$ V $: Sheet-like	83.0	85.3	57.1	35	9.15	2.32
Number Density (cm^{-3})	σ	μ	Me	Mo	K	Sk
n : All	3.16	2.86	1.10	0.11	2.25	0.78
n : Sheath-like	2.50	5.44	5.50	6.94	2.19	0.10
n : Lobe-like	0.29	0.16	0.10	0.05	258	12.5
n : Sheet-like	0.62	0.30	0.19	0.14	81.0	8.25

Table 1
Continued

Ion Temperature (eV)	σ	μ	<i>Me</i>	<i>Mo</i>	<i>K</i>	<i>Sk</i>
T_i : All	379	290	112	41	6.93	2.07
T_i : Sheath-like	47.6	72.6	59.7	41	93.3	5.15
T_i : Lobe-like	328	311	190	174	9.03	2.39
T_i : Sheet-like	429	807	733	557	2.76	0.59
Electron Temperature (eV)	σ	μ	<i>Me</i>	<i>Mo</i>	<i>K</i>	<i>Sk</i>
T_e : All	96.6	59.1	20.9	13	30.6	4.25
T_e : Sheath-like	9.67	15.3	14.3	13	7027	56.9
T_e : Lobe-like	91.4	66.8	39.3	31	41.1	4.93
T_e : Sheet-like	144	172	132	74	13.2	2.48
Temperature Ratio	σ	μ	<i>Me</i>	<i>Mo</i>	<i>K</i>	<i>Sk</i>
T/T_e : All	3.63	5.86	5.04	3.68	15.5	2.51
T/T_e : Sheath-like	2.48	4.96	4.42	3.51	6.56	1.39
T/T_e : Lobe-like	4.91	6.34	5.02	2.98	12.4	2.41
T/T_e : Sheet-like	3.06	6.12	5.52	4.77	17.7	2.65
Specific Entropy (nPa cm⁵)	σ	μ	<i>Me</i>	<i>Mo</i>	<i>K</i>	<i>Sk</i>
s_i : All	0.348	0.183	0.017	0.0019	18.9	3.42
s_i : Sheath-like	0.006	0.005	0.003	0.0019	207	7.75
s_i : Lobe-like	0.312	0.257	0.168	0.0974	21.7	3.58
s_i : Sheet-like	0.485	0.528	0.379	0.0021	8.17	1.97

Note. Shown are the standard deviation (σ), mean (μ), median (*Me*), mode (*Mo*), Pearson kurtosis (*K*), and skewness (*Sk*) for the range of the ARTEMIS observations as displayed in Figure 7. Note that the modes are rounded to the nearest integer, except for the number density, temperature ratio, and specific entropy.

4. Discussion and Conclusions

Using more than 10 years of data from the ARTEMIS mission in orbit around the Moon, this study has investigated the properties of the terrestrial magnetotail plasma environment at distances of approximately $60R_E$ downstream of Earth. When located within Earth's down-tail magnetosphere, the lunar plasma environment is highly variable, depending on its location within the magnetotail. Lobe-like fields result in a low-density plasma environment with an approximately 10 nT field and range of plasma flow velocities, sheet-like conditions yield a weaker field magnitude and denser plasma population, and magnetosheath-like conditions are characterized by the highest densities with intermediate magnetic fields and a rapid tailward flow. Our findings can be briefly summarized as follows:

- During a typical crossing of the terrestrial magnetotail, the Moon experiences a wide range of plasma environments. These disparate regions of the down-tail magnetosphere can, to first order, be grouped into magnetosheath-like, magnetotail lobe-like, and magnetotail plasma sheet-like conditions. However, there are multiple small-scale events (including signatures of reconnection) that occur within these regions of the magnetotail, causing the local lunar plasma environment to deviate from these more general characterizations.
- For magnetotail lobe-like conditions, the magnetic field magnitude peaks near a value of 10 nT and is almost entirely aligned with the Earthward/anti-Earthward B_x component; the values of B_y and B_z are centered near 0 nT. Near the central plasma sheet, the magnetic field minimizes in all three components, with an average magnitude below 4 nT. The field within the magnetosheath is more broadly distributed compared to within the lobes or plasma sheet, with an intermediate magnitude compared to the other two locations. For all of the observations in the tail, the north/south component of the field is, on average, shifted by 1–2 nT to slightly positive values, a signature of the orientation of Earth's magnetic field. The $\sim 4^\circ$ aberration of the magnetotail is also clearly visible in the magnetic field when comparing the distribution of the B_x and B_y components.

- Bulk flow velocities are preferentially directed anti-Earthward in the tail, especially within the magnetosheath and for the most frequent observations within the lobes, but this preference is reduced in the plasma sheet. Rapid Earthward and anti-Earthward plasma flows are, at times, detected near the Moon (even when located within the magnetotail lobes), which likely indicate variability in the location of the tail reconnection region.
- Plasma number densities vary by more than an order of magnitude near the Moon when located in the magnetotail, but the low-density lobes, intermediate-density sheet, and high-density magnetosheath are each clearly distinguishable. Plasma temperatures are also well-separated within the magnetotail, with the magnetosheath plasma much cooler than the lobes, which is cooler than the extended tail to the distribution of the temperatures within the central plasma sheet.

To illustrate the variability of the lunar magnetotail plasma environment in a different manner, Figure 8 displays heatmaps of the Alfvénic Mach number as a function of plasma beta. The panels display these quantities for the conditions defined in Section 3: (8a) all ARTEMIS observations over the 10-year mission, (8b) magnetosheath-like conditions only, (8c) magnetotail lobe-like conditions only, and (8d) magnetotail plasma sheet-like conditions only. As visible in panel 8a, the Alfvénic Mach number of the ambient magnetotail plasma spans multiple orders of magnitude near the Moon's orbit, ranging from decidedly sub-Alfvénic with $M_A < 10^{-3}$ to super-Alfvénic conditions with $M_A > 10^2$. Similarly, the plasma beta displays a variability of nearly five orders of magnitude, from $10^{-2} \leq \beta \leq 10^3$, and shows a generally positive correlation with the Alfvénic Mach number. Panel 8b illustrates that the fast flows and enhanced densities of the magnetosheath population are responsible for the extrema in the values of the Alfvénic Mach number and plasma beta in panel 8a, visible as a thin ridge extending to the largest values of M_A and β . Comparison of panels 8c and 8d highlight that the lobe-like plasma has, on average, a lower Alfvénic Mach number and plasma beta (with median values of $M_A = 0.07$ and $\beta = 0.09$) than near the magnetotail plasma sheet (with median values of $M_A = 0.39$ and $\beta = 7.29$).

To place the variability of the lunar plasma environment in the context of the plasma environments near various other moons throughout the solar system, Figure 8 also includes ranges of Alfvénic Mach numbers and plasma betas experienced by select outer-planet moons during their orbits around their parent planets. Displayed are ranges in M_A and β for the four Galilean moons of Jupiter in dark green, five moons of Saturn (Enceladus, Tethys, Dione, Rhea, and Titan) in orange, and Neptune's largest moon, Triton, in pink. The ranges in these plasma parameters are obtained from Kivelson et al. (2004) for the Jovian moons, from Arridge et al. (2011); Khurana et al. (2008); Krupp et al. (2020); Simon et al. (2009, 2012, 2015) for the Saturnian moons, and from Hansen et al. (2021) for Triton. We note that Artemyev, Angelopoulos, Halekas, et al. (2017) have performed a similar comparison between the plasma beta and the *magnetosonic* Mach number within the magnetotail plasma sheets of Earth and Mars (see their Figure 12). However, since we compare β to the Alfvénic Mach number, we do not include the variability of the martian plasma sheet in panel 8b.

On the one hand, Figure 8b illustrates that the magnetosheath plasma is rather unique in comparison to the environments near the outer-planet moons. Besides the most extreme cases for Callisto or Rhea, and perhaps excluding times when Titan exits Saturn's magnetosphere entirely and is exposed to the Saturnian magnetosheath and solar wind plasma (e.g., Bertucci et al., 2008, 2015; Feyerabend et al., 2016), the Moon is exposed to a higher beta, higher Alfvénic-Mach-number plasma than any of these other moons.

On the other hand, Figures 8c and 8d illustrate that the lunar plasma environment is at times similar to the plasma environments of the outer-planet moons. The terrestrial magnetotail lobe environment (panel 8c) is not too dissimilar from that experienced by Saturn's inner moons, which are exposed to the low beta, low Mach-number plasma of the Saturnian magnetosphere. Of these, Tethys, Dione, and Rhea lack dense global exospheres and their interactions with the Saturnian plasma generate plasma absorption features—including a cavity in the plasma density and magnetic field compression signatures—and Alfvén wings that extend from the moons, connecting them with the polar Saturnian ionosphere (e.g., Khurana et al., 2008; Simon et al., 2015). Further similarities in the lunar magnetotail lobe plasma can be extended to Triton—whose interaction with the markedly sub-Alfvénic and highly variable plasma environment may generate previously undetected Alfvén wing plasma absorption signatures (Liuzzo, Paty, et al., 2021; Simon et al., 2021), as well as to Io and Europa—which orbit within the strongly magnetized inner magnetosphere of Jupiter. Indeed, similar plasma interaction features well-known at these outer-planet moons have also been observed by ARTEMIS during individual encounters with the Moon while located within the magnetotail lobes (e.g., Liuzzo, Poppe, et al., 2021; Xu et al., 2019). Near the plasma

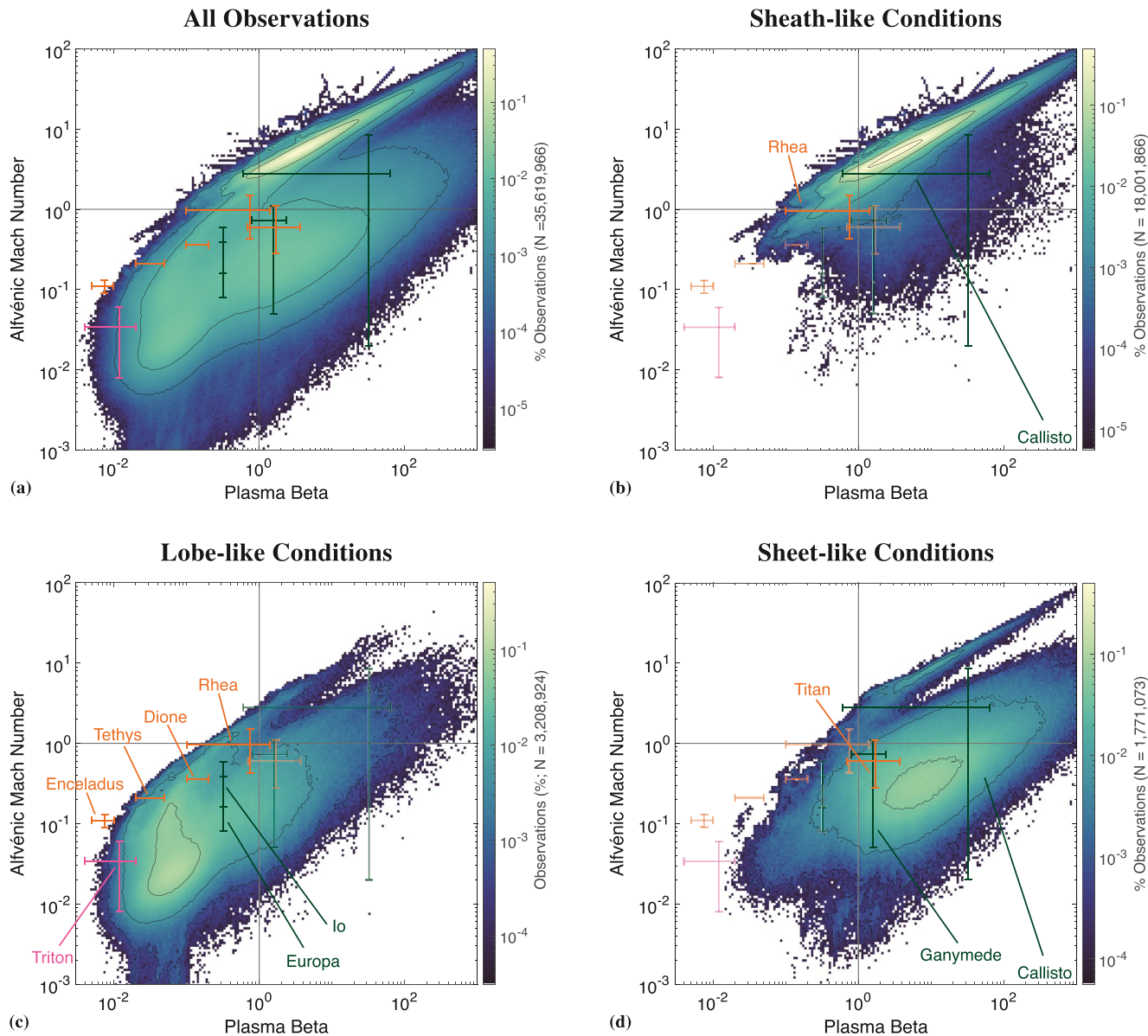


Figure 8. Heatmaps of the Alfvenic Mach number as a function of plasma beta observed by Acceleration, Reconnection, Turbulence, and Electrodynamics of the Moon's Interaction with the Sun when located within Earth's magnetotail for (a) all conditions, (b) magnetosheath-like conditions, (c) magnetotail lobe-like conditions, and (d) magnetotail plasma sheet-like conditions. Overplots are ranges of M_A and β experienced by select moons of (dark green) Jupiter, (orange) Saturn, and (pink) Neptune's moon Triton.

sheet of the terrestrial magnetotail, Figure 8d shows that the high-beta lunar plasma environment resembles the plasma to which Titan, Ganymede, and Callisto are exposed. While typical values of β and M_A are highly variable near these objects—especially near Callisto where these plasma properties span approximately three orders of magnitude—they cover much of the parameter space that is encountered by the Moon when located near the terrestrial plasma sheet.

However, while the Alfvenic Mach numbers and plasma betas may be similar near the Moon and these outer-planet satellites, significant differences exist between the terrestrial magnetotail and the outer-planet magnetospheres. One such difference arises from the orientation of the magnetospheric flow compared to the direction of the local magnetic field. Near the moons of Jupiter and Saturn, the ambient plasma flow is nearly always perpendicular to the direction of the magnetospheric background field. Near Neptune's moon Triton, the local magnetospheric field is never tilted by more than 43° against the direction of corotation (Cochrane et al., 2022;

Liuzzo, Paty, et al., 2021). In comparison, the ambient plasma flow near Earth's Moon when located within a lobe of the terrestrial magnetotail is almost entirely aligned with the direction of the tail field. While the plasma flow may be perpendicular to the local field during an individual ARTEMIS encounter (see, e.g., the case study by Liuzzo, Poppe, et al. [2021]), Figure 7 and Table 1 illustrate that on average, the plasma flow component parallel to the field dominates the perpendicular components (i.e., $V_x \gg V_y, V_z$), at least within the lobes.

An additional difference between these environments is driven by the internal dynamics of the giant planet magnetospheres. The rapid rotations of Jupiter and Saturn cause their magnetospheric plasma to continuously bombard the trailing hemispheres of the outer-planet moons, which are therefore nearly always exposed to an ambient plasma that drifts past their surfaces at a velocity $|V| \gg 0$ (reaching up to ~ 300 km/s at Jupiter's moon Callisto). In contrast, when located within the plasma sheet, for example, the terrestrial Moon is rather exposed to a low-velocity plasma that may not preferentially originate from any direction: as visible in Figure 7 and Table 1, the mean and median values for all three components of the flow velocity within the sheet are near 0 km/s. During these conditions, the lunar surface is exposed to a warm ambient plasma that surrounds the Moon and lacks any strong, directed flow, unlike the corotating plasma of the outer-planet magnetospheres. Besides, Io's volcanoes (at Jupiter) and Enceladus' plumes (at Saturn) act as a continual source of neutral particles to the magnetospheres of their parent planets, thereby affecting global magnetospheric dynamics; Earth's magnetosphere is not influenced by any analogous processes. Further differences stem from the fact that the largest outer planet moons possess either appreciable ionospheres (in the case of Titan, Triton, and Callisto) or strong internal magnetic fields (in the case of Ganymede) that affect their local electromagnetic environments. Hence, these differences likely contribute to a lunar interaction with the terrestrial plasma that is, at times, vastly different than those exhibited by the outer-planet moons.

In summary, the immense, 10-year-long ARTEMIS data set allows us to constrain the average properties of the terrestrial magnetotail plasma environment near the lunar orbit. Given the range of plasma conditions during a given magnetotail crossing, in addition to the strong variability thereof, the lunar environment may be analogous to the plasma near the outer planet moons, or unique to the magnetotail approximately $60R_E$ downstream of Earth.

Data Availability Statement

All data used for this study can be obtained from the ARTEMIS homepage (artemis.ssl.berkeley.edu) or at NASA's CDAWeb (cdaweb.gsfc.nasa.gov).

Acknowledgments

The authors acknowledge support from NASA/LDAP Grant 80NSSC20K0311. The ARTEMIS mission is funded and operated under NASA grant NAS5-02099. We thank J. P. McFadden for use of ESA data, J. E. Bonnell and F. Mozer for use of EFI data, and K.-H. Glassmeier, U. Auster, and W. Baumjohann for the use of FGM data provided under the lead of the Technical University of Braunschweig and with financial support through the German Ministry for Economy and Technology and the German Center for Aviation and Space, Contract 50-OC-0302. The authors are particularly grateful for discussions with V. Angelopoulos, D. Sibeck, S. Simon, and J. Z. D. Mieth that have strengthened the quality of this study. We appreciate input from two anonymous reviewers that have improved the study.

References

- Angelopoulos, V. (2008). The THEMIS mission. *Space Science Reviews*, 141(1–4), 5–34. <https://doi.org/10.1007/s11214-008-9336-1>
- Angelopoulos, V. (2011). The ARTEMIS mission. *Space Science Reviews*, 165(1–4), 3–25. <https://doi.org/10.1007/s11214-010-9687-2>
- Arridge, C. S., André, N., Bertucci, C. L., Garnier, P., Jackman, C. M., Németh, Z., et al. (2011). Upstream of Saturn and Titan. *Space Science Review*, 162(1–4), 25–83. <https://doi.org/10.1007/s11214-011-9849-x>
- Artemyev, A. V., Angelopoulos, V., Halekas, J. S., Runov, A., Zelenyi, L. M., & McFadden, J. P. (2017). Mars's magnetotail: Nature's current sheet laboratory. *Journal of Geophysical Research: Space Physics*, 122(5), 5404–5417. <https://doi.org/10.1002/2017JA024078>
- Artemyev, A. V., Angelopoulos, V., Runov, A., & Vasko, I. Y. (2017). Hot ion flows in the distant magnetotail: ARTEMIS observations from lunar orbit to ~ 200 RE. *Journal of Geophysical Research: Space Physics*, 122(10), 9898–9909. <https://doi.org/10.1002/2017JA024433>
- Auster, H. U., Glassmeier, K. H., Magnes, W., Aydogar, O., Baumjohann, W., Constantinescu, D., & Wiedemann, M. (2008). The THEMIS fluxgate magnetometer. *Space Science Reviews*, 141(1–4), 235–264. <https://doi.org/10.1007/s11214-008-9365-9>
- Bame, S. J., Asbridge, J. R., Felthauer, H. E., Hones, E. W., & Strong, I. B. (1967). Characteristics of the plasma sheet in the Earth's magnetotail. *Journal of Geophysical Research*, 72(1), 113–129. <https://doi.org/10.1029/jz072i001p00113>
- Baumjohann, W. (1993). The near-earth plasma sheet: An AMPTE/IRM perspective. *Space Science Reviews*, 64(1–2), 141–163. <https://doi.org/10.1007/bf00819660>
- Behannon, K. (1968). Mapping of the Earth's bow shock and magnetic tail by Explorer 33. *Journal of Geophysical Research*, 73(3), 907–930. <https://doi.org/10.1029/ja073i003p00907>
- Behannon, K. (1970). Geometry of the geomagnetic tail. *Journal of Geophysical Research*, 75(4), 743–753. <https://doi.org/10.1029/ja075i004p00743>
- Bertucci, C., Achilleos, N., Dougherty, M. K., Modolo, R., Coates, A. J., Szego, K., et al. (2008). The magnetic memory of Titan's ionized atmosphere. *Science*, 321(5895), 1475–1478. <https://doi.org/10.1126/science.1159780>
- Bertucci, C., Hamilton, D. C., Kurth, W. S., Hospodarsky, G., Mitchell, D., Sergis, N., & Dougherty, M. K. (2015). Titan's interaction with the supersonic solar wind. *Geophysical Research Letters*, 42(2), 193–200. <https://doi.org/10.1002/2014GL062106>
- Bonnell, J. W., Mozer, F. S., Delory, G. T., Hull, A. J., Ergun, R. E., Cully, C. M., & Harvey, P. R. (2008). The electric field instrument (EFI) for THEMIS. *Space Science Reviews*, 141(1–4), 303–341. <https://doi.org/10.1007/s11214-008-9469-2>
- Borovsky, J. E., Thomsen, M. F., Elphic, R. C., Cayton, T. E., & McComas, D. J. (1998). The transport of plasma sheet material from the distant tail to geosynchronous orbit. *Journal of Geophysical Research*, 103(A9), 20297–20331. <https://doi.org/10.1029/97JA03144>

- Bosqued, J. M., Lormant, N., Rème, H., D'Uston, C., Lin, R. P., Anderson, K. A., et al. (1996). Moon-solar wind interactions: First results from the WIND/3DP Experiment. *Geophysical Research Letters*, 23(10), 1259–1262. <https://doi.org/10.1029/96GL00303>
- Cao, X., Halekas, J., Poppe, A., Chu, F., & Glassmeier, K. (2020). The acceleration of lunar ions by magnetic forces in the terrestrial magnetotail lobes. *Journal of Geophysical Research: Space Physics*, 125(6), 1–12. <https://doi.org/10.1029/2020JA027829>
- Cao, X., Halekas, J. S., Chu, F., Kistler, M., Poppe, A. R., & Glassmeier, K. (2020). Plasma convection in the terrestrial magnetotail lobes measured near the Moon's orbit. *Geophysical Research Letters*, 47(20), 0–3. <https://doi.org/10.1029/2020GL090217>
- Cochrane, C. J., Persinger, R. R., Vance, S. D., Midkiff, E. L., Castillo-Rogez, J., Luspay-Kuti, A., & Prockter, L. M. (2022). Single- and multi-pass magnetometric subsurface ocean detection and characterization in icy worlds using principal component analysis (PCA): Application to Triton. *Earth and Space Science*, 9(2), e2021EA002034. <https://doi.org/10.1029/2021EA002034>
- Cowley, S. W. (1981a). Asymmetry effects associated with the x-component of the IMF in a magnetically open magnetosphere. *Planetary and Space Science*, 29(8), 809–818. [https://doi.org/10.1016/0032-0633\(81\)90071-4](https://doi.org/10.1016/0032-0633(81)90071-4)
- Cowley, S. W. (1981b). Magnetospheric asymmetries associated with the y-component of the IMF. *Planetary and Space Science*, 29(1), 79–96. [https://doi.org/10.1016/0032-0633\(81\)90141-0](https://doi.org/10.1016/0032-0633(81)90141-0)
- Feyerabend, M., Simon, S., Neubauer, F. M., Motschmann, U., Bertucci, C., Edberg, N. J. T., et al. (2016). Hybrid simulation of Titan's interaction with the supersonic solar wind during Cassini's T96 flyby. *Geophysical Research Letters*, 43(1), 35–42. <https://doi.org/10.1002/2015GL066848>
- Gencturk Akay, I., Kaymaz, Z., & Sibeck, D. G. (2019). Magnetotail boundary crossings at lunar distances: ARTEMIS observations. *Journal of Atmospheric and Solar-Terrestrial Physics*, 182(September 2017), 45–60. <https://doi.org/10.1016/j.jastp.2018.11.002>
- Georgescu, E., Plaschke, F., Auster, U., Fornaçon, K. H., & Frey, H. U. (2011). Modelling of spacecraft spin period during eclipse. *Annales Geophysicae*, 29(5), 875–882. <https://doi.org/10.5194/angeo-29-875-2011>
- Goertz, C. K., & Baumjohann, W. (1991). On the thermodynamics of the plasma sheet. *Journal of Geophysical Research: Space Physics*, 96(A12), 20991–20998. <https://doi.org/10.1029/91ja02128>
- Grigorenko, E. E., Kronberg, E. A., Daly, P. W., Ganushkina, N. Y., Lavraud, B., Sauvad, J., & Zelenyi, L. M. (2016). Origin of low proton-to-electron temperature ratio in the Earth's plasma sheet. *Journal of Geophysical Research: Space Physics*, 121(10), 9985. <https://doi.org/10.1002/2016ja022874>
- Halekas, J. S., Brain, D. A., & Holmström, M. (2015). Moon's plasma wake. In A. Keiling, C. M. Jackman, & P. A. Delamere (Eds.), *Magnetotails in the solar system* (pp. 149–167). <https://doi.org/10.1002/9781118842324.ch9>
- Halekas, J. S., Poppe, A. R., Delory, G. T., Sarantos, M., & McFadden, J. P. (2013). Using ARTEMIS pickup ion observations to place constraints on the lunar atmosphere. *Journal of Geophysical Research*, 118(1), 81–88. <https://doi.org/10.1029/2012JE004292>
- Hansen, C. J., Castillo-Rogez, J., Grundy, W., Hofgartner, J. D., Martin, E. S., Mitchell, K., et al. (2021). Triton: Fascinating moon, likely ocean world, compelling destination! *The Planetary Science Journal*, 2(4), 137. <https://doi.org/10.3847/PSJ/abffd2>
- Hardy, D. A., Freeman, J. W., & Hills, H. K. (1976). Plasma observations in the magnetotail. In *Magnetospheric particles and fields* (pp. 89–98). https://doi.org/10.1007/978-94-010-1503-5_9
- Hardy, D. A., Hills, H. K., & Freeman, J. W. (1979). Occurrence of the lobe plasma at lunar distance. *Journal of Geophysical Research*, 84(A1), 72–78. <https://doi.org/10.1029/ja084ia01p00072>
- Holmström, M., Fatemi, S., Futaana, Y., & Nilsson, H. (2012). The interaction between the Moon and the solar wind. *Earth Planets and Space*, 64(2), 237–245. <https://doi.org/10.5047/eps.2011.06.040>
- Kaymaz, Z., Siscoe, G. L., Luhmann, J. G., Lepping, R. P., & Russell, C. T. (1994). Interplanetary magnetic field control of magnetotail magnetic field geometry: IMP 8 observations. *Journal of Geophysical Research*, 99(A6), 11113–11126. <https://doi.org/10.1029/94ja00300>
- Khurana, K. K., Russell, C. T., & Dougherty, M. K. (2008). Magnetic portraits of Tethys and Rhea. *Icarus*, 193(2), 465–474. <https://doi.org/10.1016/j.icarus.2007.08.005>
- Kiehas, S. A., Runov, A., Angelopoulos, V., Hietala, H., & Korovincksiy, D. (2018). Magnetotail fast flow occurrence rate and dawn-dusk asymmetry at XGSM ~60 RE. *Journal of Geophysical Research: Space Physics*, 123(3), 1767–1778. <https://doi.org/10.1002/2017JA024776>
- Kivelson, M., Bagenal, F., Kurth, W., Neubauer, F., Paranicas, C., & Saur, J. (2004). Magnetospheric interactions with satellites. In: *Jupiter: The planet, satellites and magnetosphere*, (pp. 513–536).
- Krupp, N., Kotova, A., Roussos, E., Simon, S., Liuzzo, L., Paranicas, C., et al. (2020). Magnetospheric interactions of Saturn's moon Dione (2005–2015). *Journal of Geophysical Research: Space Physics*, 125(6), e2019JA027688. <https://doi.org/10.1029/2019JA027688>
- Lavraud, B., Borovsky, J. E., Génot, V., Schwartz, S. J., Birn, J., Fazakerley, A. N., Wild, J. A. (2009). Tracing solar wind plasma entry into the magnetosphere using ion-to-electron temperature ratio. *Geophysical Research Letters*, 36(18), L18109. <https://doi.org/10.1029/2009GL039442>
- Liuzzo, L., Paty, C., Cochrane, C., Nordheim, T., Luspay-Kuti, A., Castillo-Rogez, J., & Prockter, L. (2021). Triton's variable interaction with Neptune's magnetospheric plasma. *Journal of Geophysical Research: Space Physics*, 126(11), e2021JA029740. <https://doi.org/10.1029/2021JA029740>
- Liuzzo, L., Poppe, A. R., Halekas, J. S., Simon, S., & Cao, X. (2021). Investigating the Moon's interaction with the terrestrial magnetotail lobe plasma. *Geophysical Research Letters*, 48(9), 1–11. <https://doi.org/10.1029/2021GL093566>
- Matsumoto, Y., Mukai, T., Saito, Y., Kokubun, S., & Hoshino, M. (2001). On the pressure balance in the distant magnetotail. *Journal of Geophysical Research*, 106(A11), 25905–25917. <https://doi.org/10.1029/2001ja900064>
- McFadden, J., Carlson, C., Larson, D., Bonnell, J., Mozer, F., Angelopoulos, V., & Auster, U. (2008). THEMIS ESA first science results and performance issues. *Space Science Reviews*, 141(1–4), 477–508. <https://doi.org/10.1007/s11214-008-9433-1>
- McFadden, J., Carlson, C., Larson, D., Ludlam, M., Abiad, R., Elliott, B., et al. (2008). The THEMIS ESA plasma instrument and in-flight calibration. *Space Science Reviews*, 141(1–4), 277–302. <https://doi.org/10.1007/s11214-008-9440-2>
- Meng, C.-I., & Anderson, K. A. (1974). Magnetic field configuration in the magnetotail near 60 R E. *Journal of Geophysical Research*, 79(34), 5143–5153. <https://doi.org/10.1029/JA079i034p05143>
- Michel, F. C. (1968). Lunar wake at large distances. *Journal of Geophysical Research*, 73(23), 7277–7283. <https://doi.org/10.1029/JA073i023p07277>
- Miett, J. Z. D., Fröhauff, D., & Glassmeier, K.-H. (2019). Statistical analysis of magnetopause crossings at lunar distances. *Annales Geophysicae*, 37(2), 163–169. <https://doi.org/10.5194/angeo-37-163-2019>
- Mihalov, J. D., Colburn, D. S., Currie, R. G., & Sonett, C. P. (1968). Configuration and reconnection of the geomagnetic tail. *Journal of Geophysical Research*, 73(3), 943–959. <https://doi.org/10.1029/ja073i003p00943>
- Mittelholz, A., Grayver, A., Khan, A., & Kuvshinov, A. (2021). The global conductivity structure of the lunar upper and mid mantle. *Journal of Geophysical Research: Planets*, 126(11), e2021JE006980. <https://doi.org/10.1029/2021je006980>
- Ness, N. F. (1965). The magnetohydrodynamic wake of the Moon. *Journal of Geophysical Research*, 70(3), 517–534. <https://doi.org/10.1029/JZ070i003p00517>
- Ness, N. F. (1972). Interaction of the solar wind with the moon. In (pp. 347–393). https://doi.org/10.1007/978-94-009-3693-5_21

- Nguyen, G., Aunai, N., Welle, B. d., Jeandet, A., Lavraud, B., & Fontaine, D. (2021). Massive multi-mission statistical study and analytical modeling of the Earth's magnetopause: 2 – Shape and location. *Journal of Geophysical Research: Space Physics*, 12, 1–21. <https://doi.org/10.1029/2021JA029774>
- Poppe, A. R. (2019). Comment on “The Dominant Role of Energetic Ions in Solar Wind Interaction With the Moon” by Omidi et al. *Journal of Geophysical Research: Space Physics*, 124(8), 6927–6932. <https://doi.org/10.1029/2019ja026692>
- Poppe, A. R., Samad, R., Halekas, J. S., Sarantos, M., Delory, G. T., Farrell, W. M., & McFadden, J. P. (2012). ARTEMIS observations of lunar pick-up ions in the terrestrial magnetotail lobes. *Geophysical Research Letters*, 39(17), 1–6. <https://doi.org/10.1029/2012GL052909>
- Runov, A., Angelopoulos, V., Artemyev, A., Lu, S., & Zhou, X. Z. (2018). Near-Earth reconnection ejecta at lunar distances. *Journal of Geophysical Research: Space Physics*, 123(4), 2736–2744. <https://doi.org/10.1002/2017JA025079>
- Sarris, E. T., Krimigis, S. M., Lui, A. T. Y., Ackerson, K. L., Frank, L. A., & Williams, D. J. (1981). Relationship between energetic particles and plasmas in the distant plasma sheet. *Geophysical Research Letters*, 8(4), 349–352. <https://doi.org/10.1029/GL008i004p00349>
- Sibeck, D. G., & Murphy, K. R. (2021). Large-scale structure and dynamics of the magnetosphere. In (Vol. 2, pp. 15–36). <https://doi.org/10.1002/9781119815624.ch2>
- Sibeck, D. G., Siscoe, G. L., Slavin, J. A., & Lepping, R. P. (1986). Major flattening of the distant geomagnetic tail. *Journal of Geophysical Research*, 91(A4), 4223–4237. <https://doi.org/10.1029/JA091A04p04223>
- Sibeck, D. G., Siscoe, G. L., Slavin, J. A., Smith, E. J., Tsurutani, B. T., & Lepping, R. P. (1985). The distant magnetotail's response to a strong interplanetary magnetic field B_y : Twisting, flattening, and field line bending. *Journal of Geophysical Research*, 90(A5), 4011–4019. <https://doi.org/10.1029/JA090iA05p04011>
- Simon, S., Addison, P., & Liuzzo, L. (2021). Formation of a displaced plasma wake at Neptune's moon Triton. *Journal of Geophysical Research: Space Physics*, 127(1), e2021JA029958. <https://doi.org/10.1029/2021JA029958>
- Simon, S., Kriegel, H., Saur, J., Wennmacher, A., Neubauer, F. M., Roussos, E., Dougherty, M. K. (2012). Analysis of Cassini magnetic field observations over the poles of Rhea. *Journal of Geophysical Research*, 117(A7), A07211. <https://doi.org/10.1029/2012ja017747>
- Simon, S., Roussos, E., & Paty, C. (2015). The interaction between Saturn's moons and their plasma environments. *Physics Reports*, 602, 1–65. <https://doi.org/10.1016/j.physrep.2015.09.005>
- Simon, S., Saur, J., Neubauer, F. M., Motschmann, U., & Dougherty, M. K. (2009). Plasma wake of Tethys: Hybrid simulations versus Cassini MAG data. *Geophysical Research Letters*, 36(4), L04108. <https://doi.org/10.1029/2008GL036943>
- Slavin, J. A., Smith, E. J., Sibeck, D. G., Baker, D. N., Zwickl, R. D., & Akasofu, S.-I. (1985). An ISEE 3 study of average and substorm conditions in the distant magnetotail. *Journal of Geophysical Research*, 90(A11), 10875–10895. <https://doi.org/10.1029/ja090i11p10875>
- Vasko, I. Y., Petrukhovich, A. A., Artemyev, A. V., Nakamura, R., & Zelenyi, L. M. (2015). Earth's distant magnetotail current sheet near and beyond lunar orbit. *Journal of Geophysical Research: Space Physics*, 120(10), 8663–8680. <https://doi.org/10.1002/2015JA021633>
- Wang, C.-P., Gkioulidou, M., Lyons, L. R., & Angelopoulos, V. (2012). Spatial distributions of the ion to electron temperature ratio in the magnetosheath and plasma sheet. *Journal of Geophysical Research*, 117(A8), A08215. <https://doi.org/10.1029/2012ja017658>
- Wang, C.-P., Liu, Y. H., Xing, X., Runov, A., Artemyev, A., & Zhang, X. (2020). An event study of simultaneous earthward and tailward reconnection exhaust flows in the Earth's midtail. *Journal of Geophysical Research: Space Physics*, 125(6), e2019JA027406. <https://doi.org/10.1029/2019JA027406>
- Wang, C.-P., Lyons, L. R., & Angelopoulos, V. (2014). Properties of low-latitude mantle plasma in the Earth's magnetotail: ARTEMIS observations and global MHD predictions. *Journal of Geophysical Research: Space Physics*, 119(9), 7264–7280. <https://doi.org/10.1002/2014JA020060>
- Wing, S., Johnson, J. R., Chaston, C. C., Echim, M., Escoubet, C. P., Lavraud, B., et al. (2014). Review of solar wind entry into and transport within the plasma sheet. *Space Science Reviews*, 184(1–4), 33–86. <https://doi.org/10.1007/s11214-014-0108-9>
- Xu, X., Xu, Q., Chang, Q., Xu, J., Wang, J., Wang, Y., & Angelopoulos, V. (2019). ARTEMIS observations of well-structured lunar wake in subsonic plasma flow. *The Astrophysical Journal*, 881(1), 76. <https://doi.org/10.3847/1538-4357/ab2e0a>
- Yamamoto, T., Shiokawa, K., & Kokubun, S. (1994). Magnetic field structures of the magnetotail as observed by GEOTAIL. *Geophysical Research Letters*, 21(25), 2875–2878. <https://doi.org/10.1029/94GL01609>
- Zhang, H., Khurana, K. K., Kivelson, M. G., Angelopoulos, V., Wan, W. X., Liu, L. B., & Liu, W. L. (2014). Three-dimensional lunar wake reconstructed from ARTEMIS data. *Journal of Geophysical Research: Space Physics*, 119(7), 5220–5243. <https://doi.org/10.1002/2014JA020111>
- Zhou, X.-Z., Angelopoulos, V., Poppe, A. R., & Halekas, J. S. (2013). ARTEMIS observations of lunar pickup ions: Mass constraints on ion species. *Journal of Geophysical Research*, 118(9), 1766–1774. <https://doi.org/10.1002/jgre.20125>
- Zwickl, R. D., Baker, D. N., Bame, S. J., Feldman, W. C., Gosling, J. T., Hones, E. W., & Slavin, J. A. (1984). Evolution of the Earth's distant magnetotail: ISEE 3 electron plasma results. *Journal of Geophysical Research*, 89(A12), 11007–11012. <https://doi.org/10.1029/JA089iA12p11007>